Transport and storage of anthropogenic C in the Subpolar North Atlantic : Model – Data comparison

Virginie Racapé[1,2], Patricia Zunino[3], Pascale Lherminier[2], Herlé Mercier[3], Laurent Bopp[1,4], Fiz F. Pérèz[5] and Marion Gehlen [1]

[1]LSCE/IPSL, Laboratoire des Sciences du Climat et de l'environnement, CEA-CNRS-UVSQ, Orme des Merisiers, Bât. 712, CEA/Saclay, 91190 Gif-sur-Yvette, Cedex, France

[2]IFREMER, Laboratoire d'Océanographie Physique et Spatiale, UMR 6523, CNRS-IFREMER-IRD-UBO, Plouzané, France

[3]CNRS, Laboratoire d'Océanographie Physique et Spatiale, UMR 6523, CNRS-IFREMER-IRD-UBO, Plouzané, France

[4]Département de Géosciences, Ecole Normale Supérieure, 24 rue Lhomond 75005 Paris

[5]Instituto de Investigaciones Marinas, CSIC, Eduardo Cabello 6, 36208 Vigo, Spain

Corresponding author : Virginie Racapé, virginie.racape@ifremer.fr

Abstract

The North Atlantic Ocean is a major sink region for anthropogenic carbon (Cant) and a major contributor to its storage. While it is in general agreed that the intensity of the meridional overturning circulation (MOC) modulates uptake, transport and storage of Cant in the North Atlantic Subpolar Ocean, processes controlling their recent variability and 21st century evolution remain uncertain. This study aims to investigate the relationship between the transport of Cant, the air-sea anthropogenic CO_2 fluxes and the storage of Cant in the North Atlantic Subpolar Ocean over the past 44 years. Its relies on the combined analysis of an annual to multi-annual in situ data set and output from a global biogeochemical ocean general circulation model (NEMO/PISCES) at ½° spatial resolution forced by the atmospheric reanalysis Drakkar Forcing Set 4. Despite an underestimation of Cant transport and an overestimation of anthropogenic air-sea CO_2 fluxes in the model, Cant storage rate, its variability and driving processes are well simulated. At the interannnual time scale, this study confirms that the time rate of changes in Cant storage in NEMO/PISCES is controlled by the divergence of the northward transport of Cant between 25°N and the Greenland-Iceland-Scotland sills. Our results highlight the key role played by the divergence of the NACW transport to the storage of Cant in the upper oceanic layer of the subtropical region and to supply IW then NADW. In addition, this study shows that Cant uptake by NADW in the lower limb of the MOC mainly occurs in the OVIDE-sills box and only one quarter is exported to the subtropical region. Finally, at the multi-decadal scale, the long-term changes in the

north Atlantic Cant storage rate is rather driven by the increasing air-sea fluxes of anthropogenic CO_2.

1. Introduction

Since the start of the industrial era and the concomitant rise of atmospheric CO_2, the ocean sink and inventory of anthropogenic carbon (Cant) have increased substantially (e.g. Sabine et al., 2004; Le Quéré et al., 2009; 2014; Khatiwala et al., 2013). Overall, the ocean has absorbed 28 ± 5% of all anthropogenic CO_2 emissions, thus providing a negative feedback to global warming and climate change (Ciais et al., 2013). Uptake and storage of Cant are, however, characterized by a significant variability on interannual to decadal time scales (Le Quéré et al., 2015; Wanninkhof et al., 2013) and any global assessment will hide important regional differences, which hampers the detection of changes in the ocean sink in response to global warming and unabated emissions (Séférian et al., 2014; McKinley et al., 2016).

The North Atlantic Ocean is a key region for Cant uptake (e.g. Sabine et al., 2004; Mikaloff-Fletcher et al., 2006; Gruber et al., 2009) and stores currently as much as 20% of the total oceanic inventory of 155±31 PgC (Khatiwala et al., 2013). Uptake and enhanced storage of Cant in this region result from the combination of two processes: (1) winter deep convection in the Labrador and Irminger Seas, which efficiently transfers Cant from surface waters to the deep ocean (Körtzinger et al. 1999; Sabine et al., 2004; Pérez et al., 2008) and (2) the northward transport of warm and Cant-laden tropical waters by the upper limb of the meridional overturning circulation (MOC; e.g. Àlvarez et al., 2004; Mikaloff-Fletcher., 2006; Gruber et al., 2009; Pérez et al., 2013). Both terms, deep-water formation and circulation, are characterized by high temporal variability in response to the leading mode of atmospheric variability in the North Atlantic, the North Atlantic Oscillation (NAO). Hurrell (1995) defined the NAO index as the normalized sea-level pressure difference in winter between the Azores and Iceland. A positive (negative) NAO phase is characterized by a high (low) pressure gradient between these two systems coupled to strong (weak) westerly winds in the subpolar region. Between the mid-1960s and the mid-1990s, the North Atlantic evolved from a negative to positive NAO phase. The change in wind conditions induced an acceleration of the North Atlantic Current (NAC), as well as increased heat loss and vertical mixing in the subpolar gyre (e.g. Dickson et al., 1996; Curry and McCartney, 2001; Sarafanov, 2009; Delworth and Zeng, 2015). Concomitant enhanced deep convection led to the formation of large volumes of Labrador Sea water (LSW) with a high load of Cant (Lazier et al., 2002; Pickart et al., 2003; Pérez et al., 2008; 2013). Between 1997 and the yearly 2010's, the region undergoes a decline in NAO index. This has caused a reduction of LSW formation (Yashayaev, 2007; Rhein et al., 2011) and a slowing down of the northward transport of subtropical water by the NAC (Häkkinen and Rhines, 2004; Bryden et al., 2005; Pérez et al., 2013). As a result, the increase in the subpolar Cant inventory is below that expected from rising atmospheric anthropogenic CO_2 levels alone (Steinfeldt et al., 2009; Pérez et al., 2013).

Based on the analysis of a time series of physical and biogeochemical properties between 1997 and 2006, Pérez et al. (2013) proposed that Cant storage rates in the subpolar gyre are primarily controlled by the MOC intensity. A reduction in the MOC intensity would thus lead to a decrease in Cant storage and would give rise to a positive climate-carbon feedback. The importance of MOC in modulating the North Atlantic Cant inventory was previously suggested by model studies. Those projected a decrease in the North Atlantic Cant inventory over the 21st century in response to a projected MOC slow-down under future climate warming (e.g. Maier-Reimer et al. 1996; Crueger et al., 2008; Schwinger et al., 2014). Based on the same section than Pérez et al. (2013), Zunino et al. (2014) extended the time window of analysis to 1997-2010 and proposed a novel proxy for Cant transport. It is defined as the difference of the Cant concentration between the upper and the lower limbs of the overturning circulation times MOC intensity (see section S1 in Supplement for a model-based discussion of the proxy). They observed that while the multi-annual variability of transport of Cant at the OVIDE section was controlled by the variability of MOC intensity, its long-term change could depend on the increase in Cant concentration in the upper limb of the MOC. As the latter reflects uptake of Cant through air-sea gas exchange at the atmosphere-ocean boundary, it questions the dominant role of ocean dynamics in controlling Cant storage in the subpolar gyre at the decadal time scale (Pérez et al., 2013). If the storage rate of Cant in the subpolar gyre is indeed at first order controlled by the load of Cant in the upper limb of the MOC, the subpolar Cant inventory is expected to increase along with increasing atmospheric CO_2 - albeit not necessarily at the same rate - and to provide a negative feedback on rising atmospheric CO_2 levels over the 21st century.

The objective of the present study is to evaluate the relationship between Cant transport, air-sea fluxes and storage rate in the Subpolar North Atlantic, along with their combined evolution over the past 44 years (1958-2012). It relies on the combination of an annual to multi-annual data set gathered from 25°N to the Greenland-Iceland-Scotland sills over the period 2003-2011 and output from the global biogeochemical ocean general circulation model NEMO/PISCES at 1/2° spatial resolution forced by an atmospheric reanalysis (Bourgeois et al., 2016). The paper is organized as follow: NEMO/PISCES and *in situ* data sets are detailed in Sect. 2 and compared in Sect. 3 to evaluate the model performance; main results of the interannual to decadal change of the North Atlantic Cant fluxes and storage rate as well as the evaluation of their main drivers are presented in Sect. 4 and discussed in Sect. 5 regarding model-data comparison.

2. Material and methods

2.1. NEMO-PISCES model

This study is based on a global configuration of the ocean model system NEMO (Nucleus For European Modelling of the Ocean) version 3.2 (Madec, 2008). The quasi-isotropic tripolar grid ORCA (Madec and Imbard, 1996) has a resolution of 0.5° in longitude and 0.5° x cos(ϕ) in latitude (ORCA05) and 46 vertical levels whereof 10 levels lie in the upper 100m. It is coupled online to the Louvain-la-Neuve sea ice model version 2 (LIM2) and the biogeochemical model PISCES-v1 (Pelagic interaction Scheme for Carbon and Ecosystem studies; Aumont and Bopp, 2006). Parameter values and numerical options for the physical model follow Barnier et al. (2006) and Timmermann et al. (2005). Two atmospheric reanalysis products, DFS4.2 and DFS4.4, were used for this study. DFS4.2 is based on ERA-40 (Brodeau et al., 2010) and covers the period 1958-2007 while DFS4.4 is based on ERAInterim (Dee et al., 2011) and covers the years 2002-2012. The simulation was spun up over a full DFS4.2 forcing cycle (50 years) starting from rest and holding atmospheric CO_2 constant to levels of the year 1870 (284 ppm). Temperature and salinity were initialized as in Barnier et al. (2006). Biogeochemical tracers were either initialized from climatologies (nitrate, phosphate, oxygen, dissolved silica from the 2001 World Ocean Atlas, Conkright et al. (2002); preindustrial dissolved inorganic carbon (C_T) and total alkalinity (A_T) from GLODAP, Key et al. (2004)), or from a 3000 year long global NEMO/PISCES simulation at 2° horizontal resolution (Iron and dissolved organic carbon). The remaining biogeochemical tracers were initialized with constant values.
At the end of the spin-up cycle, two 143-year long simulations were started in 1870 and run in parallel. The first one, the historical simulation, was forced with spatially uniform and temporally increasing atmospheric CO_2 concentrations (Le Quéré et al., 2014). In the second one, the natural simulation, the mole fraction of CO_2 was kept constant in time at 284 ppm. Both runs were forced by repeating 1.75 cycles of DFS4.2 interannually varying forcing over 1870 to 1957. Then DFS4.2 was used from 1958 to 2007. Simulations were extended from 2002 to 2012 by switching to DFS4.4. No significant differences were found in tracer distributions and Cant related quantities between both atmospheric forcing products during the years of overlap (2002-2007). Carbonate

chemistry and air-sea CO_2 exchanges were computed by PISCES following the Ocean Carbon Cycle Model Intercomparison Project protocols (www.ipsl.jussieu.fr/OCMIP) and the gas transfer velocity relation provided by Wanninkhof (1992). Because climate change trends and natural modes of variability are part of the forcing set used to force both simulations, potential alterations of the natural carbon cycle in response to climate change (e.g. rising sea surface temperature) are thus also captured by the natural simulation. The concentration of anthropogenic C, as well as anthropogenic CO_2 fluxes is calculated as the difference between the historical (total C = natural + anthropogenic contribution) and the natural simulations following Orr et al. (2017).

The global ocean inventory of Cant simulated by the model in 2010 amounted to 126 PgC. It is at the lower end of the uncertainty range of the estimate by Khatiwala et al. (2013) of 155±31 PgC (Fig. 1). At the global scale, the error of the model is close to 6% (values excluding arctic regions and marginal seas). The mismatch between the modeled Cant inventory and that of Khatiwala et al. (2013) is largely explained by the difference in the starting year of integration: 1870 for this study as opposed to 1765 in Khatiwala et al. (2013). The coupled model configuration is referred to as ORCA05-PISCES hereafter. The reader is invited to refer to Bourgeois et al. (2016) for a detailed description of the model and the simulation strategy.

2.2. Observation data sets

Observations used to evaluate Cant transport computed from ORCA05-PISCES in the North Atlantic Ocean were collected along the Greenland-Portugal OVIDE section and at 24.5°N following the tracks presented on Fig. 2. Model output of air-sea CO_2 fluxes are compared to the observation-based gridded sea surface pCO_2 product of Landschützer et al. (2015a). Programs and/or data sets are briefly summarized below.

OVIDE data set

The OVIDE program aims to document and understand the origin of the interannual to decadal variability in circulation and properties of water masses in the Subpolar North Atlantic in the context of climate change (http://www.umr-lops.fr/Projets/Projets-actifs/OVIDE). Since 2002, one spring-summer cruise is run every two years (Table 1) between Greenland and Portugal (Fig. 2) Dynamical (ADCP), physical (temperature, T and salinity, S) and biogeochemical (e.g. alkalinity, A_T, pH, dissolved oxygen, O_2, and nutrients) properties are sampled at full depth hydrographic stations spaced by 25 nautical miles (NM). The spacing is reduced to 16 NM in the Irminger sea and to 12 NM or less over steep topographic features. An overview of instruments, analytical methods and accuracies of each parameter is summarized in Zunino et al. (2014). The concentration of C_T is calculated from pH and A_T following the recommendations and guidelines from Velo et al. (2010). The OVIDE data set is distributed as part of GLODAPv2 (Olsen et al., 2016) (Table 1).

24.5°N data set

Data were collected along 24.5°N in 2011 between January 27th and March 15th as part of the Malaspina circumnavigation expedicion (https://www.expedicionmalaspina.es/) (Table 1). A total of 167 full depth hydrographic stations, whereof 13 were in the Florida Straits, were sampled along the transect, spaced by 27 NM or less across the boundary currents and topographic slopes [Hernández-Guerra et al., 2014]. As for the OVIDE program, ADCP, T, S, A_T, pH, O_2 and nutrients were sampled during the cruise and CT was calculated from A_T and pH. For details on methods and accuracies, please refer to Hernández-Guerra et al. (2014) for dynamical and physical properties and to Guallart et al. (2015) for the carbonate system. This data set is made available by GO-SHIP and delivered by CCHDO (Table 1).

For both data sets, C_T is combined with T, S, nutrients, O_2 and A_T to derive the Cant concentration following the φC_T method which fix the preindustrial xCO_2 in 278.8 ppm to computed the preindustrial C_T (Pérez et al., 2008; Vàzquez-Rodrìguez et al., 2009). This data-based diagnostic approach uses water mass properties of the subsurface layer between 100-200m as reference to evaluate preformed and disequilibrium conditions. The random propagation of errors associated with input parameters yields an uncertainty of 5.2 µmol kg^{-1} on Cant values (Pérez et al., 2010). An intercomparison between different methods to separate the anthropogenic component Cant from the background of C_T carried out in the Atlantic Ocean (Vàzquez-Rodrìguez et al., 2009) and along 24.5°N (Guallart et al., 2015) concluded on a good agreement between φC_T and the other methods.

pCO_2 data base

The gridded sea surface pCO_2 product of Landschützer et al. (2015a) was created using the SOCATv2 dataset (Bakker et al., 2014) and a 2-step neural network method detailed in Landschützer et al. (2015b). It consists of monthly surface ocean pCO_2 values from 1982 to 2011 at a spatial resolution of 1°x1°. Total air-sea CO_2 fluxes were derived from equation 1 where dCO_2 is defined as the difference of CO_2 partial pressures between the atmosphere and surface ocean, *Kw* is the gas transfer velocity and *sol,* the CO_2 solubility.

$$FCO_2^{sea-air} = Kw \times sol \times dCO_2 \qquad (1)$$

As explain in Landschützer et al. (2014), *Kw* was computed as a function of wind speed following

Wanninkhof (1992) rescaled to a global mean gas transfer velocity of 16 cm h^{-1} and using winds from ERA-interim (Dee et al. 2011). s*ol* was computed following Weiss (1974) as a function of sea surface temperature (Reynolds et al., 2002 and Hadley center EN4 sea surface salinity (Good et al. 2013).

2.3. <u>Diagnostic of Cant transport and budget</u>

<u>*Transport of Cant across a section*</u>

The simulated transport of Cant (T_{Cant}) across a section has been evaluated either from online diagnostics (computed when the simulation is performed) or offline diagnostics (obtained after the simulation is finished, and computed using model outputs of velocities and concentrations). The transport of Cant is the sum of advective, diffusive and eddy terms. These terms are integrated vertically from bottom to surface and horizontally from the beginning (*A*) to the end (*B*) of a section along a continuous line defined by zonal (*y*) or meridional (*x*) grid segment (Fig. S2). Positive values stand for northward and/or eastward transport (see Sect. S2 in Supplement for the description of section). The advective term corresponds to the product of velocities orthogonal to the section (*V*) times the concentration of Cant (*[Cant], Eq. 2*).

$$^{m}T_{CANT}^{adv} = \int_{A}^{B}\int_{bottom}^{surface} V[Cant]dxydz \qquad (2)$$

The diffusive term corresponds to the transport of Cant due to the horizontal diffusion. The eddy transport is based on the parameterization of Gent and McWilliams (1990). While the online approach allows quantifying the contribution of each component, we only derived the advective term from the offline approach. We diagnosed all terms of T_{Cant} over 2003-2011, which is the only period for which the online diagnostics were available, to compare simulated T_{Cant} with the observation-based estimates from 24.5°N to the Greenland-Iceland-Scotland sills (section 3.1), and verify that the advection term was the dominant one. To study the long-term variability of Cant fluxes and storage rates (section 3.2), the time window of analysis was next extended to 1958-2012 and Cant transport was derived offline from yearly averaged model outputs according to equation 2. These estimations were completed by the heat transport along the section computed from velocities orthogonal to the section (*V*) and the heat term provided by the international thermodynamic equations of seawater (TEOS 2010).

<u>*Budget of Cant in the North Atlantic Ocean*</u>

The budget of Cant was computed for three North Atlantic sub-regions (see below for definition of regions). The budget was defined as the balance between i) the time rate of change in Cant, vertically and horizontally integrated, ii) the incoming and outgoing transport of Cant across boundaries of each region and iii) the anthropogenic air-sea CO_2 exchange, spatially integrated. Budget estimates were completed by the total air-sea CO_2 flux and the heat transport over 2003-2011. All terms were estimated from model output either from monthly or yearly averages depending on the period analyzed (monthly for 2003-2011; yearly for 1958-2012). Relationships between Cant fluxes and storage rates were investigated for each individual region.

3. Model evaluation over the period 2003-2011

Figure 3 summarizes the budget of Cant in the North Atlantic simulated by the model over the period 2003-2011. In order to enable the comparison of the model-derived budget to previous estimates (e.g. Jeansson et al., 2011; Pérez et al. 2013; Zunino et al., 2014, 2015a,b; Guallart et al., 2015), we defined two boxes separated by the Greenland-Portugal OVIDE section. The first one extends from 25° N to the OVIDE section and the second box extends from the OVIDE section to the Greenland-Iceland-Scotland sills. Seasonality was removed beforehand using a 12-month running filter.

In the model, over one third of Cant entering in the southern box at 25° N (0.092±0.016 PgC yr^{-1}) is transported across the OVIDE section (0.035±0.005 PgC yr^{-1}) and leaves the domain at the Greenland-Iceland-Scotland sills (0.034±0.004 PgC yr^{-1}). The outgoing flux corresponds to a net northward transport resulting from a northwards flux across the Iceland-Scotland strait (0.053±0.005 PgC yr^{-1}) and a southward flux across the Denmark strait (-0.020±0.014 PgC yr^{-1}). The remainder of the regional Cant storage is provided by the air to sea exchange with the largest values south of the OVIDE section (South: 0.156±0.008 PgC yr^{-1}; North 0.044±0.003 PgC yr^{-1}). As a consequence, 88% of the incoming Cant flux (computed as (0.092 + 0.156+0.044-0.034)/(0.092 + 0.156+0.044); Fig. 3) is stored inside the region every year, predominantly south of the OVIDE section (South : 0.216±0.019 PgC yr^{-1} ; North : 0.045±0.006 PgC yr^{-1}). In the next sections, Cant transport, anthropogenic air-sea CO_2fluxes and Cant storage rate are successively compared to published estimates and to the observations described in section 2.2 in order to evaluate the model performance and to study the long term change in Cant storage rate and its driving processes.

3.1. Advective transport of Cant

The comparison between online and offline estimates of Cant transport across the OVIDE section confirms the dominant contribution of advection (Fig. S3), suggested already by Tréguier et al.

(2006). Compared to previous studies, our simulated transport of Cant (Fig. 3) is nevertheless clearly underestimated: it is three times smaller at 25° N and at the OVIDE section (Pérez et al., 2013; Zunino et al., 2014, 2015a and b) and 1.5 to 2 times smaller at the sills (Jeansson et al., 2011, Pérez et al., 2013). The net Cant flux entering the OVIDE box through the Denmark strait is only one third of the estimation of Jeansson et al. (2011), whereas the outgoing flux at the Iceland-Scotland strait is only half. The following paragraphs focus on mass transport and concentration of Cant (equation 2) in order to identify the causes of the significant underestimation of modeled T_{Cant}.

<u>*Mass transport across the Greenland-Portugal OVIDE section and 25°N*</u>

The analysis of the stream function simulated by ORCA05-PISCES along the Greenland-Portugal OVIDE section reveals a general pattern that is very similar to that estimated from observation (Fig. 4). The model does not, however, reproduce the interannual variability present in the observations (Figs. 4a and 4b). Moreover, the magnitude of MOC (see Sect. S1 for details of its estimation) computed for the month of June from model output (13.4±0.6 Sv), comparable to the annual average values (12.7±0.6 Sv), is underestimated by around 2 Sv (dated-based estimate: 15.5±2.3 Sv, Mercier et al., 2015; Table 2). The upper limb of the MOC, the NAC (Lherminier et al., 2010), flows northeastward in the Eastern part of the section (East of 1100 km; Fig. 4b), with its modified branch, the Irminger Current, in the Western part (around 700km off the Greenland Coast) in model and data as defined by Mercier et al. (2015) (Fig. 4b). The NAC is simulated with a lower variability and weaker intensity (Fig. 4b; ORCA05-PISCES increase in cumulative volume transport of 15 Sv instead of 25 Sv between 1100km and 2500km from Greenland coast). In addition, the vertical stream function (Fig. 4a) reveals a stronger current between the surface and the density anomaly (σ_1) 31.5 kg m^{-3} in the model, only observed at the east of the Reykjanes Ridge (not show here). This overestimation of the overturning stream function in the model is likely due to a shift in the position of the Western limit of the NAC. The Western limit is identified by close to zero values for volume transport. It occurs around 1000 km off Greenland in the model, instead of 1300 km in observations (Fig. 4b).

The lower limb of MOC, mainly related to the Western Boundary Current (WBC), flows southward in the western part of the section (Lherminier et al., 2007; 2010; Mercier et al., 2015). Sigma 1 separating both limbs of the MOC simulated by the model is lower (32.01±0.01 kg m^{-3}) than estimated from *in situ* data (32.14 kg m^{-3}). It follows that the lower (upper) limb in the model takes up a bigger (smaller) volume along the section compared to the OVIDE data set (Fig. 5). The model underestimates the intensity of the southward transport of the WBC in the Irminger Sea, and the East Reykjanes Ridge current in the Iceland basin (Fig. 4b), which are the most intense currents flowing in the lower limb of the MOC. It also underestimates the cumulative volume transport for σ_1 >32.40 kg m^{-3} (σ_0 >27.7 kg m^{-3}), which is close to 0 Sv in the model (Fig. 4a) as opposed to 7 Sv recorded by Lherminier et al. (2007) and García-Ibáñez et al. (2015). These densest water masses correspond to lower North East Atlantic Deep Water (lNEADW), Denmark Strait Overflow Water (DSOW) and Iceland Scotland Overflow Water (ISOW). Taken together, the misfit between observation-derived estimates and modeled volume transport is largest in the Irminger and Iceland basins. This suggests that the significant underestimation of volume transport in the highest density classes is probably due to the close to zero contribution of overflow waters to the transport in the model at the latitude of the OVIDE section.

At 25°N, the upper limb of the MOC, composed by North Atlantic Central Water (NACW), Antarctic Intermediate Water (AAIW) and Mediterranean Water (MW) (Talley et al., 2008; Hernández-Guerra et al., 2014), flows northward with an intensity of 8.99±2.28 Sv in the model from January through March 2011 (Fig. 6a). The lower limb, transporting southward North Atlantic Deep Water (NADW) and northward Antarctic Bottom Water (AABW; Kuhlbrodt et al., 2007; Talley et al., 2008; Fig. 6b), is characterized by a net maximal flux of -10.82±2.14 Sv (Fig. 6a) detected at the density level (σ1) 31.95±0.00 kg m^{-3}. While there is a large seasonal variability (Fig. 6b), the magnitude of the winter MOC (10.82±2.14 Sv) is representative of the annual value in 2011 (11.59±1.86; Table 3) and over 2003-2011 (11.13±0.80; Table 3). The intensity of simulated MOC is weaker (Table 3) and the limit between upper and lower limb is shallower (Fig. 7) than results reported by Hernández-Guerra et al., (2014) (20.1±1.4 Sv at γ_n = 27.82 or σ1 = 32.27) for the same period, as well as reported by McCarthy et al. (2012) at 26°N between 2005 and 2008 (18.5±1.0 Sv). McCarthy et al. (2012) highlighted nevertheless a decline in MOC intensity of 30% over the period 2009-2010 mainly due to the increase in the southward upper ocean recirculation (shallower than 1100m) and the decrease in the southward transport of lower (l)NADW. lNADW is essentially made up of Nordic overflow waters (Pickart, 1992; Smethie et al., 2000), which the model fails to reproduce correctly. The preceding suggests that the underestimation of the volume transport in the model is likely due to the large underestimation of dense overflow waters.

Cant distribution in the North Atlantic Ocean and along the OVIDE section and 25°N

Compared to the observation-based product of Khatiwala et al. (2013), Cant concentrations simulated by ORCA05-PISCES are relatively well represented from 25°N to the Greenland-Iceland-Scotland sills (Fig. 1). Minimum values are found in the subtropical region whereas the maximum values are simulated in the subpolar gyre, especially in the Labrador Sea. Figure 1 points nevertheless to an under-estimation of up to 40 molC m^{-2} of modeled maxima. The comparison between modeled and observed Cant along the Greenland-Portugal OVIDE section and 25°N reveals a comparable distribution with higher concentrations in surface waters and lower levels at depth (Figs. 5 and 7). The surface to depth gradient is more pronounced in the Eastern basin of two sections. Along the OVIDE section (Figs. 5a and b), the two LSW cores, relatively rich in Cant, are identified on the two sides of the Reykjanes Ridge. Despite the good agreement of spatial patterns, modeled concentrations are lower by 6.3±0.6 µmol kg^{-1} compared to observed-based estimates (Table 2). Half of this underestimation is due to the preindustrial atmospheric CO_2 condition used by the model (284 ppm) compared to φCT method (278.8 ppm). This deficit is more pronounced in the upper limb of MOC (ΔCant$^{\text{model-data}}$ = -5.9±0.7 µmol kg^{-1}) than in the lower limb (ΔCant$^{\text{model-data}}$ = -3.6±0.6, Table 2). The largest difference between model and data (up to -20 µmol kg^{-1}, Fig. 5c) is detected in subsurface waters at the transition between East North Atlantic Central Water (ENACW) and Mediterranean Water (MW) and between both limbs of the MOC.

The variability of the model-data difference, diagnosed as its standard deviation, peaks at 10 µmol kg^{-1} (Fig. 5d). It is largest at the boundary between upper and lower limbs of the MOC, mainly between 700 km to 2000 km off Greenland. The higher variability in this region could be explained by the variability of the NAC intensity, which is underestimated by ORCA05-PISCES.

Figure 5 also reveals an underestimation by the model of Cant levels in NEADWl (below 3500m depth in the western European basin) by 5 to 10 µmol kg^{-1} which is in line with a close to zero contribution of dense Cant rich overflow waters along the OVIDE section.

At 25°N, a subsurface pool of Cant is detected in the western part of the section in both products (Figs. 7a and b) around 1500m depth, albeit with smaller concentrations in the model. The model underestimates the Cant concentration, especially in the lower limb of the MOC with mean values of 2.89±0.09 µmol kg^{-1} compared to 12.00 µmol kg^{-1} calculated from observations (Table 3). The largest difference between ORCA05-PISCES and observations, up to -30 µmol kg^{-1}, is found around 500m depth in the upper limb of the MOC. Finally and like along the OVIDE section, Fig. 7 reveals an under-estimation of Cant levels below 3500m depth by about 10 µmol kg^{-1}. This water mass corresponds to AABW that becomes NEADW during its northward transport by mixing with lNADW (Talley et al., 2008).

From the preceding follows that the underestimation of Cant transport in ORCA05-PISCES is likely due to the underestimation of water mass transport intensity (mainly attributed to a too weak contribution of dense overflow waters) and of Cant concentrations. The hypothesis is supported by the analysis of the heat transported at 25° N and the OVIDE section, which is also underestimated by the model (Fig. 3) compared to Pérez et al (2013). Pérez et al. (2013) estimated a heat transport of 1.10±0.01 PW and 0.59±0.09 PW at 25° N and OVIDE, respectively, while the model yields a corresponding heat transport of 0.78±0.06 PW and 0.39±0.02 PW. The discrepancy between model and observation-based estimates of heat transport is, however, not as large as for the advective transport of Cant, probably due to a better representation of temperature than Cant concentration by the model (mean model-data bias along the section:-0.4±0.9°C for a mean value of 5°C (8% of error) for temperature, 7 µmol kg^{-1} for a mean value of 25.4 µmol kg^{-1} (27%) for Cant).

3.2. Air-sea fluxes of total and anthropogenic CO_2

Estimates of modeled air-sea fluxes of total and anthropogenic CO_2 are higher than those derived from *in situ* data by Pérez et al. (2013) : Southern box: model = (anth) 0.156 ± 0.008 PgC yr^{-1} / (total) 0.303 ± 0.013 PgC yr^{-1}, Pérez et al. (2013) = (anth) 0.12±0.05 PgC yr^{-1} / (total) 0.20 PgC yr^{-1}; Northern box: model = (anth) 0.044 ± 0.003 PgC yr^{-1} / (total) 0.103 ± 0.006 PgC yr^{-1}, Pérez et al. (2013) = (anth) 0.016±0.012 PgC yr^{-1} / (total) 0.09 PgC yr^{-1} . While the model overestimates CO_2 uptake, the ratio anthropogenic/natural is comparable to Gruber et al. (2009) and Schuster et al. (2013). As a consequence, the model overestimates both natural and anthropogenic components with quite similar proportion. To understand the large over-estimation of fluxes, simulated average air-sea fluxes of total CO_2 over the period 2003-2011 are next compared to estimates by Landschützer et al., (2015a), taken as a representative observation-based product from the SOCOM exercise (Rödenberk et al. 2015). The area extending from 25°N to the Greenland-Iceland-Scotland sills is a sink for atmospheric CO_2 in the model and the data-based product (Fig.8). Three areas present nevertheless differences from observations. The first one is located south of Newfoundland and centered at 35°W-45°N. In this region, which corresponds to the NAC path in the observations (see figure 1 in Daniault et al., 2016), modeled total air-sea CO_2 fluxes are around 0 molC m^2 yr^{-1} compared to values up to -3.5 molC m^2 yr^{-1} reported in Landschützer et al. (2015a). The second area is found close to the Western African coast, where the model simulates a CO_2 source to the atmosphere shifted to the north and extending more to the west along 25°N than in observations. The third zone that differs from observations is the northern box between the OVIDE section and the Greenland-Iceland-Scotland sills. Here, the modeled oceanic CO_2 sink is overestimated in average by a factor of 2 to 3. Panels 8c and 8d show the month of the maximum, respectively minimum value of air-sea CO_2 flux for the period 2003-2011. It reveals a seasonal phase shift between ORCA05-PISCES and Landschützer et al. (2015a), north of 50°N where the model over-estimates strongly gas exchange. Fluxes peak in winter in observations while they are at a maximum in summer in the model. According to Takahashi et al. (2002), the seasonal change in surface water pCO_2 is dominated by the biological effect north of 40°N and by the temperature (or thermodynamic) effect between 20°N and 40°N. The main driving process of seasonal variability of air-sea CO_2 fluxes is well reproduced by the model in the subtropical region. However, the dominant effect of temperature extends too far north in the model. As a result, the seasonal change in CO_2 fluxes is dominated by the thermodynamic effect in the subpolar gyre. Despite the seasonal phase shift noted in the subpolar gyre, the amplitude of the interannual variability of total air-sea CO_2 fluxes (standard deviation of the 1982-2011 time series without seasonality, Fig. 9) is well reproduced by the model over the total domain and even north of 40°N where the variability is the largest.

3.3. Storage rate of Cant

The storage rates of Cant estimated for the period 2003-2011 are close to the estimates from Pérez et al. (2013), referenced to 2004: Southern box: model = 0.216 ± 0.019, Pérez et al. (2013) = 0.280±0.011; Northern box: model = 0.045 ± 0.006 and Pérez et al. (2013) = 0.045±0.004 PgC yr^{-1}. These results suggest that there may be a compensation in the model between the underestimation of Cant transport and the overestimation of anthropogenic air-sea CO_2 fluxes detailed above. Next, the contribution of air-sea uptake and transport of Cant to the variability of the North Atlantic Cant inventory is derived for each box from the analysis of multi-annual time series of anthropogenic air-sea CO_2 fluxes, transport divergence of Cant (defined as the difference between incoming and outgoing Cant fluxes at the borders of the boxes) and Cant storage rate. Time series were smoothed as explained previously and the potential trends were removed. Correlation coefficient (r) and p-value are summarized in table 4. Our results suggest that, over the period 2003-2011, the rate of Cant storage between 25° N and the Greenland-Iceland-Scotland sills is strongly correlated with a positive transport divergence of Cant (25° N: r = 0.96, p-value = 0.00; OVIDE: r = 0.95, p-value = 0.00). The dominance of Cant transport divergence over gas exchange is corroborated by observation-based assessments (Pérez et al., 2013; Zunino et al., 2014; 2015a and b). Despite an underestimation of Cant transport and an overestimation of anthropogenic air-sea CO_2 fluxes, modeled storage rate, its variability and driving processes are coherent with observations allowing the simulation to be used to study drivers of changes in Cant storage rate since 1958.

4. Cant fluxes and storage rate in the North Atlantic Ocean (North of 25°N) since 1958

In this section, we present the analysis of the full period covered by our simulations (1958-2012) with the objective of better understanding the interannual to decadal variability of the Cant inventory in the North Atlantic Ocean as well as its driving processes. The study area, from 25°N to the Greenland-Iceland-Scotland sills, is divided in 3 boxes instead of 2 in section 3: the first box extends from 25°N to 36°N; the second box from 36°N to the OVIDE section and the third box is between the OVIDE section and the Greenland-Iceland-Scotland sills. The section 36°N was added to delimit the northern part of the subtropical region from the Subpolar gyre (Mikaloff-Fletcher et al., 2003).

4.1. Contribution of variability of circulation and Cant accumulation on Cant transport variability

Figure 10 presents annual time series (1958-2012) of the magnitude of the MOC and transports of heat and Cant at 25°N, 36°N and across the OVIDE section. The heat transport and the MOC intensity are strongly correlated at each section (25°N, r = 0.92, p-value = 0.00; 36° N, r=0.90, p-value = 0.00; OVIDE, r=0.76, p-value = 0.00) whereas a significant relationship between the MOC strength and the Cant transport is only found at 36°N (25°N, r= 0.30, p-value = 0.02; 36°N, r=0.67, p-value = 0.00; OVIDE, r=0.02, p-value = 0.90). As expected, the circulation is thus the major driver of interannual to decadal variability of heat transferred across these sections (Johns et al., 2011, Mercier et al., 2015). Its impact on the variability of Cant transport is, however, masked by several other mechanisms. The transport of Cant across the three sections is characterized by a continuous increase over the period of study (Fig. 10): it increases from 0.030±0.002 PgC yr^{-1} in 1958-60 to 0.095±0.024 PgC yr^{-1} in 2010-12 at 25°N, from 0.009±0.001 PgC yr^{-1} to 0.050±0.018 PgC yr^{-1} at 36°N and from 0.008±0.001 PgC yr^{-1} to 0.043±0.005 PgC yr^{-1} at the OVIDE section. Such a large increase is observed neither on the heat transport (0.0003±0.0004 PW yr^{-1} at 25°N, 0.0016±0.0004 PW yr^{-1} at 36° N and 0.0003±0.0002 PW yr^{-1} at OVIDE) nor on the MOC magnitude (0.001±0.005 Sv yr^{-1} at 25°N, 0.015±0.006 Sv yr^{-1} at 36° N and 0.003±0.007 Sv yr^{-1} at OVIDE), nor on the net volume of water transported across the sections (-0.000 ±0.000 Sv yr^{-1} at 25°N, 0.001±0.001 Sv yr^{-1} at 36° N and -0.000 ±0.003 Sv yr^{-1} at OVIDE). Following Zunino et al. (2014), we conclude that the increase in the northward transport of Cant since 1958 was mainly due to Cant accumulation in the northward flowing upper limb of the MOC. In order to isolate the effect of circulation, we removed the positive trend from Cant transport time series. The correlation (r) between the detrended Cant transport and the magnitude of the MOC increased from 0.30 (p-value = 0.02) to 0.74 (p-value = 0.00) at 25°N and from 0.67 (p-value = 0.00) to 0.70 (p-value = 0.00) at 36°N. It did not change at the OVIDE section (r=0.1, p-value = 0.4). We conclude that the circulation controls the interannual to decadal variability of Cant transport but only at 25°N and 36°N. In the following section, we study the impact of circulation on Cant storage rate regarding the

Cant transport *divergence*.

4.2. <u>Interannual to decadal variability of the North Atlantic Cant inventory</u>

Figure 11 provides the budget of Cant from 1959 to 2011 for the three boxes. Each budget is composed of the Cant storage rate, the anthropogenic air-sea CO_2 flux and the transport divergence of Cant. We observe a continuous increase in the North Atlantic Cant inventory over the last 44-years, especially in box 2 (36°N-OVIDE) where the storage rate is multiplied by 3 (from 0.043±0.000 PgC yr^{-1} (1959-1961) to 0.127±0.010 PgC yr^{-1} (2009-11)) and in box 1 (25°N-36°N) where it doubled (from 0.039±0.000 PgC yr^{-1} to 0.094±0.004 PgC yr^{-1}). Taking into account the anthropogenic perturbation in the surface layer and assuming the transient steady-state, we expected a factor of 2.9 that is in line with and validate our result in box 2. Air-sea flux of Cant and Cant transport divergence contribute equally to changes in Cant inventory in the southern box. Between 36°N and the OVIDE section, the contribution of gas exchange dominates prior to 1985. Since 1985, the transport divergence gained in importance, albeit with a pronounced interannual variability. In the northern box, changes in Cant inventory follow air-sea fluxes (weak contribution of transport divergence limited to interannual variability).

The significant positive correlation (Table 5a, no trend removed) between storage rate and air-sea gas exchange in all three boxes suggests the latter to be, over the past 42 years, a main control of Cant storage rate on the longer time scales. Nevertheless, the transport divergence of Cant in the southern box and between 36°N and the OVIDE section from 1985 onward, which increased continuously over the period, also correlates with the change in Cant storage rate (Table 5a, trend included). It did not however influence the long-term change in Cant inventory between the OVIDE section and the Greenland-Iceland-Scotland sills (OVIDE-Sills; r = 0.32, p-value = 0.02; Table 5), where it is close to zero (incoming T_{Cant} = outgoing T_{Cant}). In this analysis (correlation with trend included), the trend in response to increasing atmospheric CO_2 levels dominates the signal and the correlation at the expense of interannual variability. In order to identify controls of the interannual variability, the analysis was repeated with detrended time series. It reveals a strong correlation between the Cant storage rate and the transport divergence of Cant for all three boxes (Table 5b), as opposed to correlation with air-sea gas exchange which is either not significant or weak (Table 5b). The model output analysis suggests that while the long term changes in Cant storage rate are controlled by anthropogenic air-sea CO_2 fluxes, its interannual variability is on the contrary driven by the transport divergence of Cant. Additional analyses are made to identify which role is played by the circulation in the annual evolution of Cant storage rate. In this context, we estimated for each box the correlation between the detrended time series of Cant transport divergence and the incoming and outgoing transport of Cant. These estimates, summarized in table 6, show that the transport divergence of Cant is always correlated with the incoming transport of Cant and not with the outgoing transport of Cant. Results of this section suggest that the interannual variability of the North Atlantic Cant storage rate is driven by the transport of Cant coming from south latitude. According to Sect. 4.1, the interannual changes of both terms at 25°N and 36°N depends on MOC intensity. These results corroborate the conclusion of section 3.3 for the period 2003-2011 and are in line with previous studies (Pérez et al., 2013; Zunino et al., 2014).

4.3. Contribution of advection of water masses to the storage rate of Cant

In this section, we analyze major water masses taking part to the upper and lower limb of the MOC in order to identify their contributions to the regional Cant storage rate over the period 1958-2012. The general circulation from 25°N to the Greenland-Iceland-Scotland sills is well documented (e.g. Arhan, 1990; McCartney, 1992; Hernández-Guerra et al., 2015; Daniault et al., 2016). Based on these studies and the water column distribution of zonally integrated mass transport at 25°N, 36°N, OVIDE and the Greenland-Iceland-Scotland sills (Fig. 12), we identify three water classes : North Atlantic Central Water (NACW, Class 1), Intermediate waters (IW; Class 2) and North Atlantic Deep Water (NADW, Class 3).

NACW (Class 1) is transported by the upper ocean circulation, either northward (Class 1N) by the Gulf Stream and the NAC, or southward (Class 1S) by the subtropical gyre recirculation in the western European basin. The southeastward recirculation is characterized by cool and dense waters (Talley et al., 2008) allowing distinction of Class 1S from Class 1N in our study (Fig. 12). NACW loses heat during its northward journey and becomes denser. As a result, its density limit changes with latitude (Fig. 12). Based on Fig. 12, we define the class 1N from surface to the density anomaly σ_1 = 29.1 kg m^{-3} at 25°N, 30 kg m^{-3} at 36°N and 31 kg m^{-3} at the OVIDE section. This class is not found at the Greenland-Iceland-Scotland sills. The class 1S, proper to the subtropical region, is found from 29.1 kg m^{-3} to 31 kg m^{-3} at 25°N and from 30 kg m^{-3} to 31 kg m^{-3} at 36°N.

IW (Class 2) encompasses the densest water masses of the upper MOC limb, such as Antarctic Intermediate Water (AAIW), Subantarctic Intermediate Water (SAIW) or Mediterranean Water (MW). The class 2 circulates northward between σ_1 = 31 and 31.8 kg m^{-3} from 25°N to OVIDE and between σ_1 = 31 and 31.9 kg m^{-3} through the Greenland-Iceland-Scotland sills (Fig. 12).

NADW (Class 3) supplies the lower limb of the MOC. It flows southward from the subpolar gyre to the subtropical region. In the model, it is found below σ_1 = 31.7-31.9 kg m^{-3} (Fig. 12).

The long term changes in simulated volume and Cant transports for these three specified classes across the four sections highlight two periods, before and after 1995. The distinction between these two periods is based on Class 1N (northward NACW) at the OVIDE section and Class 2 (IW) at 36°N where both Cant and volume transport increased after 1995 (Fig. S4). No remarks are reported on Cant storage rate in previous section. Based on these comment, we focus this section on the period 1958-1994 to understand how each water mass contributes to Cant storage rate. The period 1996-2011 is discussed is Sect. 5 to understand causes of the increase in volume and Cant transports after 1995. Results for the first period (1958-1994) are summarized on Fig. 13.

Before 1995, more than 50% of Cant transported by NACW flowing northward (Class 1N) at 25°N crossed 36°N whereas 30% recirculated southward with Class 1S. At the OVIDE section, the transport of Cant was equal to 12% of 25°N, whereas it is close to zero at the sills (Fig. 13). The transport divergences of Cant for Class 1 in Box 1 (0.034 PgC yr^{-1}= 0.096-0.056+0.022-0.028), Box 2 (0.022 PgC yr^{-1} = 0.056-0.012-0.022) and Box 3 (0.012 PgC yr^{-1} = 0.012 – 0.000) are positive and higher than Cant storage rate (Fig. 13). Figure 13 also reveals a positive anthropogenic CO_2 fluxes from atmosphere to surface Ocean. The Cant budget of Class 1 for each box suggests in fact a vertical transport of Cant from Class 1 to Class 2. Our results from this section and Sect. 4.2 indicate that the NACW plays a key role in the Cant storage rate between 25°N and the OVIDE section but also in the Cant transfer into the lower layer during its northward transport. This cross-isopycnal transport evidenced between Class 1 and Class 2 during its northward journey (Fig. 13) is related to a large decrease in the northward transport in Class 1 associated with a large increase in the northward transport in Class 2 from 25°N to the OVIDE section (Fig. S4). This is in line with results from De Boisséson et al. (2012) who highlight the densification of subtropical central water by winter air-sea cooling and mixing with intermediate waters along the NAC path. Moreover, our results from Cant transport (Fig. 13) also suggest that IW is enriched in Cant between 25°N and the OVIDE section over the studied period. The large Cant uptake north of 36°N is explained by regional winter deep convection that occurs along the NAC that mixed NACW, rich in Cant, with IW, poor in Cant. Figure 13 also shows that 64% of Cant entering into Box 3 by advection and air-sea gas exchange is exported southward by Class 3, 20% is stored whereas 16% is exported northward through the Greenland-Iceland-Scotland sills by Class 2. In addition, the budget of Cant computed for Class 2 reveals a significant vertical transport of Cant from IW to NADW, especially north of the OVIDE section. NADW is thus enriched in Cant from NACW/IW essentially between the OVIDE section and the Greenland-Iceland-Scotland sills, which is in agreement with results from Sarafanov et al. (2012). Finally, a small fraction of Cant entering in Box 2 within Class 3 leaves the area across 25°N (24%, Fig. 13). The remainder is stored within Class 3 between 25°N and OVIDE.

5. Discussion and Conclusion

The model-data comparison highlights a large underestimation (by 2 or 3 times) of the Cant transport by the model, resulting from an underestimation of both volume transport and Cant accumulation in the water column. The underestimation of the volume transport is likely due to the too small contribution of overflow waters. Their misrepresentation leads to an underestimation of the intensity of the lower limb of the MOC and as a consequence, of that of the upper branch. It results a smaller than expected export of Cant from the subtropical region to the subpolar gyre. The insignificant southward flow of overflow waters also contributes to make the net export of Cant to the Arctic region relatively large (outgoing flux at Iceland-Scotland Ridge is only divided by 2 while incoming flux at Denmark Strait is divided by 3 compared to observations). Our analysis also reveals a strong overestimation of the modeled air-sea anthropogenic CO_2 exchange. This discrepancy is associated with a larger total CO_2 uptake by the ocean north of the OVIDE section. Moreover, we observe an overestimation of the modeled anthropogenic CO_2 flux. North of 40°N, this overestimation of the total air-sea CO_2 flux is partially due to a seasonal change dominated by the thermodynamic effect rather than the biological effect. While anthropogenic CO_2 exchange as defined in the model is not impacted by the biological activity, thermodynamic mechanism affect positively anthropogenic CO_2 fluxes. The overestimation of the modeled anthropogenic air-sea CO_2 fluxes could also be a response to the low Cant concentration in the North Atlantic surface Ocean due to the model initial condition and the small Cant fraction transported inside the subpolar gyre that enhanced the air-sea anthropogenic pCO_2 gradient. These results are clearly a limit of the model that underestimates the contribution of Cant transport to storage rate. This is especially true for the OVIDE-Sills box where we observe an unexpected transport divergence close to zero (no contribution) along with an overestimation of the air-sea flux. The modeled Cant storage rate is, however, in line with data-based estimates that reflect a compensation between the underestimation of Cant transport and the overestimation of air-sea gas exchange. The spatial distribution of Cant storage is well reproduced by the model. In line with independent studies (Sabine et al., 2004; Khatiwala t al., 2013), the North Atlantic Ocean, north of 25°N, acts as a sink for the atmospheric anthropogenic CO_2, a large part of which being stored between 36°N and the OVIDE section. Moreover, mechanisms controlling the interannual to decadal changes in Cant storage rate as well as Cant and heat transport match with data-based estimates (Pérez et al., 2013; Zunino et al., 2014, 2015b; Johns et al., 2011). The satisfying reproduction of interannual variability by the model allowed its use to explore the interannual to multidecadal changes in the North Atlantic Cant

inventory and its driving processes.
At the interannual time scale, the time rate of change of Cant storage in the model is controlled by the divergence of the northward transport of Cant in the region between 25°N and the Greenland-Iceland-Scotland sills, similarly to the data-based results reported by Pérez et al. (2013) and Zunino et al. (2014; 2015b). At the OVIDE section, the interannual variability of Cant transport is controlled by Cant accumulation in the upper MOC limb whereas it is also influenced by the MOC magnitude at 25°N and 36°N. Additional analysis of the Cant transport in density classes highlights the key role played by the divergence of the NACW transport to the storage of Cant in the upper oceanic layer of the subtropical region and to supply IW then NADW. These water mass conversions are consistent with previous study (Sarafanov et al., 2012; De Boisséson et al., 2012; Pérez et al., 2013). The Cant uptake by Class-3 in the lower limb of the MOC mainly occurs in the OVIDE-sills box. A significant correlation between the volumes of NADW transported across the OVIDE section and the NAO winter index is highlighted (Fig. 14; $r = 0.68$, p-value = 0.00). A positive (negative) anomaly of volume transport is associated with a positive (negative) NAO index. Previous studies also reported an acceleration of the NAC during the transition phase period (e.g. Dickson et al., 1996; Curry and McCartney, 2011). The increase in transport of the NAC is well reproduced by the model with the anomaly of NACW mass transport being correlated with the NAO winter index (Fig. 14). This study also highlights a specific period before and after 1995 likely to explain the lack of correlation. According to Fig. 15 and S4, the period after 1995 is characterized by i) an increase in the transport of Cant and volume through the OVIDE section by NACW, ii) an increase in IW production between 25°N and 36°N but a decrease between 36°N and OVIDE associated with iii) an increase in NACW recirculation at 36°N. In the other word, since 1995, we observed more Class 1 rich in Cant advected through the OVIDE section. As shown in Fig. 16, the subpolar gyre undergoes a warming of its mixed layer since 1995. Such warming was reported by De Boisséson et al. (2012) for the year 1998. Authors explained this by an increase in the inflow of subtropical water into the Iceland basin. This enhanced advection of subtropical water into the subpolar gyre could explain the decreasing contribution of anthropogenic air-sea CO_2 fluxes to Cant storage in favor of the advective transport of Cant reported in Sect. 4.2 between 36°N and the OVIDE section. Warm, alkalinity rich subtropical waters carry a relatively high load of Cant and their enhanced northward advection decrease the air-sea gradient of anthropogenic pCO_2 and slow down air-sea gas exchange (Thomas et al., 2008).
To conclude, at the multi-decadal time scale, the long term change in anthropogenic air-sea CO_2 fluxes over the whole domain exert the dominant control on the Cant inventory of the North Atlantic subpolar gyre. The contribution of Cant transport from 25°N across the OVIDE section

emerges as the important driver on interannual to decadal time scales through its divergence. Our model analysis suggests that assuming unabated emissions of CO_2, the storage rate of Cant in the Subpolar North Atlantic is expected to increase assuming MOC fluctuations within observed boundaries. However, under a future strong decrease in MOC in response to global warming (IPCC projection 25%, Collins et al., 2013) the storage rate might decrease.

References

Álvarez, M., Pérez, F. F., Bryden, H., & Ríos, A. F. : Physical and biogeochemical transports structure in the North Atlantic subpolar gyre, J Geophys Res: Oceans, 109(C3), 2004.

Arhan, M.: The North Atlantic Current and Subartic Intermediate Water, J. Mar. Res., 48(1), 109-144, doi: 10.1357/002224090784984605, 1990.

Aumont, O., and Bopp, L.: Globalizing results from ocean in situ iron fertilization studies, Global Biogeochem Cy, 20(2), 2006.

Bakker, D. C. E., Pfeil, B., Smith, K., Hankin, S., Olsen, A., Alin, S. R., Cosca, C., Harasawa, S., Kozyr, A., Nojiri, Y., O'Brien, K. M., Schuster, U., Telszewski, M., Tilbrook, B., Wada, C., Akl, J., Barbero, L., Bates, N. R., Boutin, J., Bozec, Y., Cai, W.-J., Castle, R. D., Chavez, F. P., Chen, L., Chierici, M., Currie, K., de Baar, H. J. W., Evans, W., Feely, R. A., Fransson, A., Gao, Z., Hales, B., Hardman-Mountford,N. J., Hoppema, M., Huang, W.-J., Hunt, C. W., Huss, B., Ichikawa, T., Johannessen, T., Jones, E. M., Jones, S. D., Jutterström, S., Kitidis, V., Körtzinger, A., Landschützer, P., Lauvset, S. K., Lefèvre, N., Manke, A. B., Mathis, J. T., Merlivat, L., Metzl, N., Murata, A., Newberger, T., Omar, A. M., Ono, T., Park, G.-H., Paterson, K., Pierrot, D., Rios, A. F., Sabine, C. L., Saito, S., Salisbury, J., Sarma, V. V. S. S., Schlitzer, R., Sieger, R., Skjelvan, I., Steinhoff, T., Sullivan, K. F., Sun, H., Sutton, A. J., Suzuki, T., Sweeney, C., Takahashi, T., Tjiputra, J., Tsurushima, N., van Heuven, S. M. A. C., Vandemark, D., Vlahos, P., Wallace, D. W. R., Wanninkhof, R., and Watson, A. J.: An update to the Surface Ocean CO2 Atlas (SOCAT version 2), Earth Syst. Sci. Data, 6, 69–90, doi:10.5194/essd-6-69-2014, URL: http://www.earth-syst-sci-data.net/6/69/2014/, 2014.

Barnier, B., Madec, G., Penduff, T., Molines, J. M., Treguier, A. M., Le Sommer, J., Beckmann, A., Biastoch, A., Böning, C., Dengg, J., Derval, C., Durand, E., Gulev, S., Remy, E., Talandier, C., Theetten, S., Maltrud, M., McClean, J., and De Cuevas, B.: Impact of partial steps and momentum advection schemes in a global ocean circulation model at eddy-permitting resolution, Ocean Dynam., 56, 543–567, 2006

Bourgeois, T., Orr, J. C., Resplandy, L., Terhaar, J., Ethé, C., Gehlen, M., and Bopp, L.: Coastalocean uptake of anthropogenic carbon, Biogeosciences 13, 4167-4185, doi:10.5194/bg-13-4167-2016, 2016.

Brodeau, L., Barnier, B., Treguier, A. M., Penduff, T. and Gulev, S.: An ERA40-based atmospheric forcing for global ocean circulation models, Ocean Modelling, 31(3), 88-104, 2010.

Bryden, H. L., Longworth, H. R. and Cunningham, S. A.: Slowing of the Atlantic meridional overturning circulation at 25 N, Nature, 438(7068), 655-657, 2005.

Ciais, P., Sabine, C., Bala, G., Bopp, L., Brovkin, V., Canadell, J., Chhabra, A., Defries, R., Galloway, J., Heimann, M., Jones, C., Le Quéré, C., Myneni, R.B., Piao, S and Thornton, P.: Carbon and other biogeochemical cycles. In: Climate Change 2013: The Physical Science Basis. Contribution of Working Group I to the Fifth Assessment Report of the Intergovernmental Panel on Climate Change [Stocker, T.F., D. Qin, G-K. Plattner, M. Tignor, S.K. Allen, J. Boschung, A. Nauels, Y. Xia, V. Bex and P.M. Midgley (eds.)]. Cambridge University Press, Cambridge, United Kingdom and New York, NY, USA, 2013.

Collins, M., Knutti, R., Arblaster, J., Dufresne, J-L., Fichefet, T., Friedlingstein, P., Gao, X., Gutwoski, W.J., Johns, T., Krinner, G., Shongwe, M., Tebaldi, C., Weaver, A.J. and Wehner, M.: Long-term Climate Change: Projections, Commitments and Irreversibility. . In: Climate Change 2013: The Physical Science Basis. Contribution of Working Group I to the Fifth Assessment Report of the Intergovernmental Panel on Climate Change [Stocker, T.F., D. Qin, G-K. Plattner, M. Tignor, S.K. Allen, J. Boschung, A. Nauels, Y. Xia, V. Bex and P.M. Midgley (eds.)]. Cambridge University Press, Cambridge, United Kingdom and New York, NY, USA, 2013.

Conkright, M. E., Locarnini, R. A., Garcia, H. E., O'Brien, T. D., Boyer, T. P., Stephens, C. and Antonov, J. I.: World Ocean Database 2001: Objective analyses, data statistics and figures, 2002

Crueger, T., Roeckner, E., Raddatz, T., Schnur, R. and Wetzel, P.: Ocean dynamics determine the response of oceanic CO_2 uptake to climate change, Clim dynam, 31(2-3), 151-168, 2008.

Curry, R. G. and McCartney, M. S.: Ocean gyre circulation changes associated with the North Atlantic Oscillation, J Phys Oceanogr, 31(12), 3374-3400, 2001.

Daniault, N., Mercier, H., Lherminier, P., Sarafanov, A., Falina, A., Zunino Rodriguez, P., Pérez, F.F., Rios, A.F., Ferron, B., Huck, T., Thierry, V. and Gladyshev, S.: The northern North Atlantic Ocean mean circulation in the early 21sr century. Prog Oceanogr, 146, 142-158, doi: 10.1016/j.pocean.2016.06.007, 2016.

de Boisséson, E., Thierry, V., Mercier, H., Caniaux, G and Débruyères, D. : Origin, formation and variability of the Subpolar Mode Water located over the Reykjanes Ridge. JGR (C12005), 117, doi: 10.1029/2011JC007519, 2012

Dee, D. P., Uppala, S. M., Simmons, A. J., Berrisford, P., Poli, P., Kobayaski, S., Andrae, U., Balmaseda, M. A., Balsamo, G., Bauer, P., Bechtold, P., Beljaars, A. C. M., van de Berg, L., Bidlot, J., Bormann, N., Delsol, C., Dragani, R., Fuentes, M., Geer, A. J., Haimberger, L., Healy, S. B., Hersbach, H., Hólm, E .V, Isaksen, L., Kållberg, P., Köhler, M., Matricardi, M., McNally, A. P., Monge-Sanz, B. M., Morcrette, J.-J., Park, B.-k., Peubey, C., de Rosnay, P., Tavolato, C., Thépaut, J.-N and Vitart, F.: The ERA-Interim reanalysis: configuration and perdormance of the data assimilation system, Q. J. Roy. Meteor. Soc. 137 (656), 553-597, 2011

Delworth, T. L. and Zeng, F.: The impact of the North Atlantic Oscillation on climate through its influence on the Atlantic Meridional Overturning Circulation, J Climate, 2015.

Dickson, R., Lazier, J., Meincke, J. and Rhines, P.: Long-term coordinated changes in the convective activity of the North Atlantic. In Decadal Climate Variability (pp. 211-261). Springer Berlin Heidelberg, 1996.

García-Ibáñez, M. I, Pardo, P. C., Carracedo, L., Mercier, H., Lherminier, P., Rìos, A. F. and Pérez, F. F.: Structure, transports and transformations of the water masses in the Atlantic Subpolar Gyre, Prog. Oceanogr. 135, 18-36, doi: 10.1016/j.pocean.2015.03.009, 2015.

Gent, P. R., and Mcwilliams, J. C.: Isopycnal mixing in ocean circulation models, J Phys Oceanogr, 20(1), 150-155, 1990.

Guallart, E. F., Schuster, U., Fajar, N. M., Legge, O., Brown, P., Pelejero, C., Messias, M-J., Calvo, E., Watson, A., Ríos, A. F. and Pérez, F. F.: Trends in anthropogenic CO2 in water masses of the Subtropical North Atlantic Ocean, Progr. Oceanogr., 131, 21-32, doi: 10.1016/j.pocean.2014.11.006, 2015.

Good, S. A., Martin, M. J. and Rayner, N. A.: EN4: quality controlled ocean temperature and salinity profiles and monthly objective analyses with uncertainty estimates, J. Geophys. Res-Oceans, 118, 6704-6716, 2013

Gruber, N., Gloor, M., Mikaloff Fletcher, S. E., Doney, S. C., Dutkiewicz, S., Follows, M. J.,Gerber, M., Jacobson, A.R., Joos, F., Lindsay, K., Menemenlis, D., Mouchet, A., Muller, S.A, Sarmiento, J.L. and Takahashi, T.:. Oceanic sources, sinks, and transport of atmospheric CO_2, Global Biogeochem Cy, 23(1), 2009.

Häkkinen, S., and Rhines, P. B.: Decline of subpolar North Atlantic circulation during the 1990s, Science, 304(5670), 555-559, 2004.

Hernández-Guerra, A., Pelegrí, J. L., Fraile-Nuez, E., Benítez-Barrios, V., Emelianov, M., Pérez-Hernández, M. D., Vélez-Belchí, P.: Meridional overturning transports at 7.5N and 24.5N in the Atlantic Ocean during 1992–93 and 2010–11, Progr. Oceanogr., 128, 98–114, doi: 10.1016/j.pocean.2014.08.016, 2014.

Hurrell, J. and National Center for Atmospheric Research staff (Eds)

IOC, SCOR and IAPSO: The international thermodynamic equation of seawater - 2010: Calculation and use of thermodynamic properties. Intergovernmental Oceanographic Commission, Manuals and Guides No. 56, UNESCO (English), 196 pp. Available from http://www.TEOS-10.org. See section 3.3 of this TEOS-10 Manual, 2010.

Jeansson, E., Olsen, A., Eldevik, T., Skjelvan, I., Omar, A. M., Lauvset, S. K., Nilsen, J. E. Ø., Bellerby, R. G. J., Johannessen, T. and Falck, E.: The Nordic Seas carbon budget: Sources, sinksn and uncertainties, Global Biogeochel. Cy., 25, GB4010, doi: 10.1029/2010GB003961, 2011.

Johns, W.E., Baringer, M.O., Beal, L.M., Cunningham, S.A., Kanzow, T., Bryden, H.L., Hirschi, J.J.M., Marotzke, J., Meinen, C.S., Shaw, B., Curry, R.,: Continuous, array-based estimates of Atlantic Ocean heat transport at 26.5N, J. Climate, 24, 2429–2449, doi: 10.1175/2010JCLI3997.1, 2011.

Key, R. M., Kozyr, A., Sabine, C. L., Lee, K., Wanninkhof, R., Bullister, J. L., Feely, R. A., Millero, F. J., Mordy, C. and Peng, T.-H.: A global ocean carbon climatology: Results from Global Data Analysis Project (GLODAP), Global Biogeochem Cy 18, GB4031, doi:10.1029/2004GB002247, 2004

Khatiwala, S., Primeau, F. and Hall, T.: Reconstruction of the history of anthropogenic CO2 concentrations in the ocean, Nature, 462, 346-349, doi:10.1038/nature08526, 2009.

Khatiwala, S., Tanhua, T., Fletcher, S. M., Gerber, M., Doney, S. C., Graven, H. D., Gruber, N., McKinley, G.A, Murata, A., Rıos, A.F., and Sabine, C. L.: Global ocean storage of anthropogenic carbon, Biogeosciences, 10(4), 2169-2191, 2013.

Körtzinger, A., Rhein, M., and Mintrop, L.: Anthropogenic CO2 and CFCs in the North Atlantic Ocean-A comparison of man-made tracers, Geophys Res Lett, 26(14), 2065-2068, 1999.

Kuhlbrodt, T., Griesel, A. Montoya, M., Levermann, A., Hofmann, M. and Rahmstorf, S.: On the driving processes of the Atlantic meridional overturning circulation, Rev. Geophys, 45, RG2001, doi: 10.1029/2004RG000166, 2007.

Landschützer, P., Gruber, N. and Bakker, D. C. E. and Schuster, U.: Recent variability of the global ocean carbon sink, Global Biogeochem. Cy., 28, 947-949, doi:10.1002/2014GB004853, 2014.

Landschützer, P., Gruber, N. and Bakker, D.C.E.: A 30 years observation-based global monthly gridded sea surface pCO2 product from 1982 through 2011. http://cdiac.ornl.gov/ftp/oceans/SPCO2_1982_2011_ETH_SOM_FFN. Carbon Dioxide Information Analysis Center, Oak Ridge National Laboratory, US Department of Energy, Oak Ridge, Tennessee. doi: 10.3334/CDIAC/OTG.SPCO2_1982_2011_ETH_SOM-FFN, 2015a.

Landschützer, P., Gruber, N., Haumann, F. A., Rödenbeck, C., Bakker, D.C.E., van Heuven, S., Hoppema, M., Metzl, N., Sweeney, C., Takahashi, T., Tilbrook, B. and Wanninkhof, R.: The reinvigoration of the Southern Ocean carbon sink, Science, 349, 1221-1224. doi: 10.1126/science.aab2620, 2015b.

Lazier, J., Hendry, R., Clarke, A., Yashayaev, I. and Rhines, P.: Convection and restratification in the Labrador Sea, 1990–2000, Deep Sea Res PtI, 49(10), 1819-1835, 2002.

Le Quéré, C., Raupach, M. R., Canadell, J. G., Marland, G. and co-authors: Trends in the sources and sinks of carbon dioxide, Nature Geosciences, 2(12), 831-836, 2009.

Le Quéré, C., Peters, G. P., Andres, R. J., Andrew, R. M., and co-authors : Global carbon budget 2013, ESSD, 6, 235–263, doi:10.5194/essd-6-235-2014, 2014.

Le Quéré, C. Moriarty, R., Andrew, R.M., Peters, G.P., and co-authors: Global Carbon Budget 2014, 2015.

Lherminier, P., Mercier, H., Gourcuff, C., Alvarez, M., Bacon, S. and Kermabon, C.: Transports across the 2002 Greenland-Portugal Ovide section and comparison with 1997, J Geophys Res-Oceans, 112(C7), 2007.

Lherminier, P., Mercier, H., Huck, T., Gourcuff, C., Perez, F. F., Morin, P., Sarafanov, A., andFalina, A.: The Atlantic Meridional Overturning Circulation and the subpolar gyre observed at the A25-OVIDE section in June 2002 and 2004, Deep Sea Res Pt I 57(11), 1374-1391, 2010.

Madec, G., and Imbard, M.: A global ocean mesh to overcome the North Pole singularity, Climate Dy 12(6), 381-388, 1996.

Madec, G.: NEMO Ocean Engine, vol. 27, pp. 1–217, Note du Pole de modélisation de l'Institut Pierre-Simon Laplace, France, 2008

Maier-Reimer, E., Mikolajewicz, U. and Winguth, A. : Future ocean uptake of CO2: interaction between ocean circulation and biology, Clim. Dynam., 12(10), 711-722, doi: 10.1007/s003820050138, 1996.

McCarthy, G., Frajka-Williams, E., Johns, W. E., Baringer, M. O., Meinen, C. S., Bryden, H. L., Rayner, D., Duchez, A., Roberts, C. and Cunningham, S. A.: Observed interannual variability of the Atlantic meridional overturning circulation at 26.5°N, Geophys. Res. Lett., 39, L19609, doi:10.1029/2012GL052933, 2012

McCartney, M. S. and Talley, L. D.: The subpolar mode water of the North Atlantic Ocean, J. Phys. Oceanogr., 12(11), 1169-1188, doi : 10.1175/1520-0485(1982)012, 1982

McCartney, M. S.: Recirculation components to the deep boundary current of the northern Nort Atlantic, Prog. Oceanogr., 29(4), 283-383, doi: 10.1016/0079-6611(92)90006-L, 1992.

McKinley, G.A., Pilcher, D.J., Fay, A.R., Lindsay, K., Long, M.C. and Lovenduski, N.S.: Timescales for detection of trends in the ocean carbon sink. Nature, 530, 469-472, 2016.

Mercier, H., Lherminier, P., Sarafanov, A., Gaillard, F., Daniault, N., Desbruyères, D., Falina, A., Ferron, B., Gourcuff, C., Huck, T. and Thierry, V.: Variability of the meridional overturning circulation at the Greenland–Portugal OVIDE section from 1993 to 2010, Prog Oceanogr 132 (2015) 250–261, doi:10.1016/j.pocean.2013.11.001, 2015

Mikaloff Fletcher, S. E., Gruber, N., and Jacobson, A. R.: Ocean Inversion Project How-to Document Version 1.0, 18 pp. Institute for Geophysics and Planetary Physics, University of California, Los Angles, 2003

Mikaloff Fletcher, S. E., Gruber, N., Jacobson, A. R., Doney, S. C., Dutkiewicz, S., Gerber, M., Follows, M., Joos, F., Lindsay, K., Menemenlis, D., Mouchet, A., Müller, S.A. and Sarmiento, J.L.: Inverse estimates of anthropogenic CO_2 uptake, transport, and storage by the ocean. Global Biogeochem Cy 20(2), doi:10.1029/2005GB002530, 2006.

Olsen, A., Key, R. M., van Heuven, S., Lauvset, S. K., Velo, A., Lin, X., Schirnick, C., Kozyr, A. , Tanhua, T. , Hoppema, M. , Jutterström, S., Steinfeldt, R., Jeansson, E., Ishii, M., Pérez, F. F., and Suzuki T.: The Global Ocean Data Analysis Project version 2 (GLODAPv2) – an internally consistent data product for the world ocean, Earth Syst. Sci. Data, 8, 297–323, doi:10.5194/essd-8-297-2016., 2016

Orr, J. C., Najjar, R. G., Aumont, O., Bopp, L., Bullister, J. L., Danabasoglu, G., Doney, S. C., Dunne, J. P., Dutay, J-C., Graven, H., Griffies, S. M., John, J. G., Joos, F., Levin, I., Lindsay, K., Matear, R., McKinley, G. A., Mouchet, A., Oschlies, A., Romanou, A., Schlitzer, R., Tagliabue, A., Tanhua, T. and Yool, A.: Biogeochemical protocols and diagnostics for the CMIP6 Ocean Model Intercomparison Project (OMIP), Geosci. Model Dev., 10, 2169-2199, doi: 10.5194/gmd-10-2169-2017, 2017.

Pérez, F. F., Vazquez-Rodriguez, M., Louarn, E., Padín, X. A., Mercier, H., and Ríos, A. F. : Temporal variability of the anthropogenic CO2 storage in the Irminger Sea, Biogeosciences, 5(6), 1669-1679, 2008

Pérez, F. F., Vázquez Rodríguez, M., Mercier, H., Velo, A., Lherminier, P. and Ríos, A. F. : Trends of anthropogenic CO_2 storage in North Atlantic water masses, Biogeosciences, 7, 1789–1807, doi:10.5194/bg-7-1789-2010, 2010.

Pérez, F. F., Mercier, H., Vázquez-Rodríguez, M., Lherminier, P., Velo, A., Pardo, P. C., Roson, G., and Ríos, A. F. : Atlantic Ocean CO_2 uptake reduced by weakening of the meridional overturning circulation, Nature Geoscience, 6(2), 146-152, doi: 10.1038/NGEO1680, 2013

Pickart, R. S.: Water mass components of the North Atlantic deep western boundary current, Deep-Sea Res. Pt A, 39(9), 1553-1572, doi: 10.1016/0198-0149(92)90047-W, 1992.

Pickart, R. S., Straneo, F. and Moore, G. W. K.: Is Labrador sea water formed in the Irminger basin?, Deep Sea Res Pt I 50(1), 23-52, 2003.

Reynolds, R. W., Rayner, N. A., Smith, T. M., Stokes, D. C., and Wang, W.: An improved in situ and satellite SST analysis for climate, J. Climate, 15, 1609–1625, 2002.

Rhein, M., Kieke, D., Hüttl-Kabus, S., Roessler, A., Mertens, C., Meissner, R., Klein, B., Böning, C.W. and Yashayaev, I.: Deep water formation, the subpolar gyre, and the meridional overturning circulation in the subpolar North Atlantic, Deep-Sea Res. Pt II 58(17), 1819-1832, 2011.

Rödenbeck, C., Bakker, D. C. E., Gruber, N., Iida, Y., Jacobson, A. R., Jones, S., Landschützer, P., Metzl, N., Nakaoka, S., Olsen, A., Park, G-H, Peylin, P., Rodgers, K. B., Sasse, T. P., Schuster, U., Shutler, J. D., Valsala, V., Wanninkhof, R. and Zeng, J.: Data-based estimates of the ocean carbon sink variability – first results of the Surface Ocean pCO2 mapping intercomparison (SOCOM), Biogeosciences, 12, 7251-7278, doi: 10.5194/bg-12-7251-2015, 2015.

Sabine, C. L., Feely, R. A., Gruber, N., Key, R. M., Lee, K., Bullister, J. L., Wanninkhof, R., Wong, C.S., Wallace, D.W.R., Tilbrook, B., Millero, F.J., Peng, T-H., Kozyr, A., Ono, T. and Rios, A.F.: The oceanic sink for anthropogenic CO_2. Science 305(5682), 367-371, 2004.

Sarafanov, A.: On the effect of the North Atlantic Oscillation on temperature and salinity of the subpolar North Atlantic intermediate and deep waters. ICES Journal of Marine Science: Journal du Conseil, 66(7), 1448-1454, 2009.

Sarafanov, A., Falina, A., Mercier, H., Sokov, A., Lherminier, P., Gourcuff, C., Gladyshev, S., Gaillard, F. and Daniault, N. : Mean full-depth summer circulation and transports at the northern periphery of the Atlantic Ocean in the 2000s, J. Geophys. Res., 117(C01014), doi : 10.1029/2011JC007572, 2012.

Schuster, U., McKinley, G. A., Bates, N., Chevallier, F., Doney, S. C., Fay, A. R., González-Dávila, M., Gruber, N., Jones, S., Krijnen, J., Landschützer, P., Lefèvre, N., Manizza, M., Mathis, J., Metzl, N., Olsen, A., Rìos, A. F., Rödenbeck, C., Santana-Casiano, J. M., Takahashi, T., Wanninkhof, R., and Watson, A. J.: An assessment of the Atlantic and Arctic sea–air CO_2 fluxes, 1990–2009, Biogeosciences, 10, 607–627, doi:10.5194/bg-10-607-2013, 2013

Schwinger, J., Tjiputra, J. F., Heinze, C., Bopp, L., Christian, J. R., Gehlen, M., Ilyina, T., Jones, C. D., Salas-Mélia, D., Segschneider, J., Séférian, R. and Totterdell, I.: Nonlinearity of ocean carbon cycle feedbacks in CMIP5 Earth System Models, J. Climate, 27(11), 3869-3888, doi: 10.1175/JCLI-D-13-00452.1, 2014

Séférian, R., Ribes, A. and Bopp, L.: Detecting the anthropogenic influences on recent changes in ocean carbon uptake: Geophys. Res. Lett, 41, 5968-5977, doi: 10.1029/1999JC900274, 2014.

Smethie, W. M., Fine, R. A., Putzka, A. and Jones, E. P.: Tracing the flow of North Atlantic Deep Water using chlorofluorocarbons, J. Geophys. Res., 105(C6), 14297-14323, 2000.

Steinfeldt, R., Rhein, M., Bullister, J. L. and Tanhua, T.: Inventory changes in anthropogenic carbon from 1997–2003 in the Atlantic Ocean between 20 S and 65 N, Global Biogeochem Cy 23(3), 2009.

Takahashia, T., Sutherland, S. C., Sweeney, C., Poisson, A., Metzl, N., Tilbrook, B., Bates, N., Wanninkhof, R., Feely, R. A., Sabine, C., Olafsson, J. and Nojiri, Y.: Global sea–air CO2 flux based on climatological surface ocean pCO2, and seasonal biological and temperature effects, Deep-Sea Res. pt II, 49,1601–1622, doi: 10.1016/S0967-0645(02)00003-6, 2002.

Talley, L. D., Pickard, G. L., Emery, W. J. and Swift, J. H.: Descriptive physical oceanography: an introduction, Academic press, pp 555, 2008

Timmermann, R., Goosse, H., Madec, G., Fichefet, T., Ethe, C. and Duliere, V.: On the representation of high latitude processes in the ORCA-LIM global coupled sea ice–ocean model. Ocean Modelling, 8(1), 175-201, 2005.

Thomas, H., Prowe, F.A. E., Lima, I. D., Doney, S. C., Wanninkhof, R., Greatbach, R. J., Schuster, U. and Corbière, A.: Changes in the North Atlantic Oscillation influence CO2 uptake in the North Atlantic over the past 2 decades, Global Biogeochem. Cy., 22(4), doi: 10.1029/2007GB003167, 2008.

Treguier, A-M., Gourcuff, C., Lherminier, P., Mercier, H., Barnier, B., Madec, G., Molines, J-M., Penduff, T., Czeschel, L., Böning, C.W.: Internal and Forced variability along a section between Greenland and Portugal in the CLIPPER Atlantic model. Ocean Dynam 56 (5-6), 568-580, doi:10.1007/s10236-006-0069-y, 2006

Vázquez-Rodríguez, M., Padin, X. A., Ríos, A. F., Bellerby, R. G. J. and Pérez, F. F.: An upgraded carbon-based method to estimate the anthropogenic fraction of dissolved CO_2 in the Atlantic Ocean, Biogeosciences Discuss., 6, 4527–4571, doi:10.5194/bgd-6-4527-2009, 2009.

Velo, A., Pérez, F. F., Lin, X., Key, R. M., Tanhua, T., de la Paz, M., Olsen, A., van Heuven, S., Jutterström, S. and Ríos, A. F.: CARINA data synthesis project: pH data scale unification and cruise adjustments, Earth Syst. Sci. Data, 2, 133–155, doi:10.5194/essd-2-133-2010, 2010.

Wanninkhof, R.: Relationship between wind speed and gas exchange over the ocean, Jeophys Res 97(C5), 7373-7382, 1992.

Wanninkhof, R., Park, G.H., Takahashi, T., Sweeney, C., Feely, R.A., Nojiri, Y., Gruber, N., Doney, S.C., McKinley, G.A., Lenton, A., Le Quere, C., Heinze, C. Schwinger, J., Graven, H., and Khatiwala, S.: Global Ocean carbon uptake: Magnitude, variability and trend, Biogeosciences 10, 1983-2000, doi:10.5194/bg-10-1983-2013, 2013.

Weiss, R. F.: Carbon Dioxide in Water and Seawater: The Solubility of a Non-Ideal Gas, Mar. Chem., 2, 203–215, 1974.

Yashayaev, I.: Hydrographic changes in the Labrador Sea, 1960–2005, Prog Oceanogr 73(3), 242-276, 2007.

Zunino, P., Garcia-Ibanez, M. I., Lherminier, P., Mercier, H., Ríos, A. F. and Pérez, F. F.: Variability of the transport of anthropogenic CO2 at the Greenland-Portugal OVIDE section: Controlling mechanisms, Biogeosciences, 11, 2375–2389, doi:10.5194/bg-11-2375-2014, 2014

Zunino, P., Lherminier, P., Mercier, H., Padín, X. A., Ríos, A. F. and Pérez, F. F.: Dissolved inorganic carbon budgets in the eastern subpolar North Atlantic in the 2000s from in situ data, Geophys Res Lett 42(22), 9853-9861, 2015a.

Zunino, P., Pérez, F. F., Fajar, N. M., Guallart, E. F., Ríos, A. F., Pelegrí, J. L. and Hernández-Guerra, A.: Transports and budgets of anthropogenic CO_2 in the tropical North Atlantic in 1992–1993 and 2010–2011, Global Biogeochem Cy, 29(7), 1075-1091, 2015b.

Acknowledgments

For this work, VR was funded through the EU FP7 project CARBOCHANGE (grant 264879). Simulations were made using HPC resources from GENCI-IDRIS (grant x2015010040). We are grateful to Christian Ethé, who largely contributed to obtain Cant transport in online mode over the period 2003-2011. We want to acknowledge HM (supported by CNRS and the ATLANTOS H2020 project (GA 633211)) and colleagues for leading the OVIDE project (supported by French research institutions, IFREMER and CNRS/INSU), as well as Alonso Hernandez-guerra for the availability of its mass transport data at 24.5°N. Other data at 24.5°N used in this paper were collected and made publicly available by the International Global Ship-based Hydrographic Investigations Program (GO-SHIP; http://www.go-ship.org/) and the national programs that contribute to it. We are also grateful to N. Gruber and one anonymous reviewer for their constructive comments.

Table captures

Table 1: Summary of cruises and data set used throughout this study

OVIDE name	Month/year	Vessel	Reference	expocode
OVIDE 2002	06-07/2002	N/O Thalassa	Lherminier et al., 2007	35TH20020611
OVIDE 2004	06-07/2004	N/O Thalassa	Lherminier et al., 2010	35TH20040604
OVIDE 2006	05-06/2006	R/V Maria S. Merian	Gourcuff et al., 2011	06MM20060523
OVIDE 2008	06-07/2008	N/O Thalassa	Mercier et al. 2015	35TH20080610
OVIDE 2010	06-07/2010	N/O Thalassa	Mercier et al., 2015	35TH20100608
24.5°N-2011	01-03/2011	Sarmiento de Gamboa	Hernández-Guerra et al. 2014	29AH20110128

Table 2: Model-data comparison over the period covered by the OVIDE cruises (2002-2010). Average and standard deviation (SD) for observation-based estimates (column 2) and model output (columns 3 to 4). Model output: (1) June average with SD being a measure of interannual variability and (2) average year with SD corresponding to the average interannual variability.

	OVIDE data set	ORCA05-PISCES	
		June only	**average year**
MOCσ (sv)	15.5±2.3	13.4±0.6	12.7±0.6
σMOC (kg m^{-3})	32.14	32.02±0.05	31.95±0.04
$[Cant]_{section}$ (µmol kg^{-1})	25.4±1.8	18.4±1.1	18.4±1.1
$[Cant]_{upper}$ (µmol kg^{-1})	45.2±3.0	38.9±3.0	39.4±3.0
$[Cant]_{lower}$ (µmol kg^{-1})	19.4±1.6	14.8±1.0	14.9±1.0

Table 3: Model-data comparison along 25°N. Average and standard deviation (SD) for observation-based estimates (column 2) and model output (columns 3 to 5). Model output: (1) January from March 2011 average with SD being a measure of winter variability, (2) average 2011 year with SD corresponding to the average seasonal variability and (3) average 2003-2011 year with SD being representative of interannual variability.

	24.5°N data set	ORCA05-PISCES		
		Winter only	**Average 2011 year**	**Average 2003-2011 year**
MOCσ (sv)	20.1±1.4	10.82±2.14	11.59±1.86	11.13±0.80
σMOC (kg m^{-3})	32.27	31.95±0.00	32.02±0.03	32.00±0.03
$[Cant]_{section}$ (µmol kg^{-1})	19.73	8.69±0.02	8.73±0.04	
$[Cant]_{upper}$ (µmol kg^{-1})	40.36	39.15±0.01	38.86±0.90	
$[Cant]_{lower}$ (µmol kg^{-1})	12.00	2.89±0.1	2.86±0.08	

Table 4: Correlation coefficient (r) and p-value between the time rate of change (Trate), the divergence of Cant transport (DT_{Cant}) and air sea Cant fluxes (F_{Cant}) for the two boxes, 25°N-OVIDE and OVIDE-Sills, over the period 2003-2011. DT_{Cant} = incoming – outgoing Cant fluxes across the boundaries of boxes.

Box 25° N to OVIDE	
	Trate/DT_{Cant} : r = 0.96, p-value = 0.00
	Trate/F_{Cant} : r = - 0.54, p-value = 0.00
Box OVIDE to sills	
	Trate/DT_{Cant} : r = 0.95, p-value = 0.00
	Trate/F_{Cant} : r = - 0.71, p-value = 0.00

Table 5: Correlation coefficient (r) and p-value between the time rate of change (Trate) of Cant

storage, the divergence of Cant transport (DT_{Cant}) and air sea Cant fluxes (F_{Cant}) for the three boxes, 25°N-36°N, 36°N-OVIDE and OVIDE-Sills, over the period 1959-2011. DT_{Cant} = incoming – outgoing Cant fluxes across the boundaries of boxes. The analyses were done, first, with the original time series (left column in the table) and after, with the detrended Cant transport time series (right column in the table).

a. Including trend	b. without trend
Box 25° N to 36°N	**Box 25° N to 36°N**
Trate/DT_{Cant} : r = 0.93, p-value = 0.00	Trate/DT_{Cant} : r = 0.94, p-value = 0.00
Trate/F_{Cant} : r = 0.90, p-value = 0.00	Trate/F_{Cant} : r = 0.04, p-value = 0.78
Box 36°N to OVIDE	**Box 36°N to OVIDE**
Trate/DT_{Cant} : r = 0.73, p-value = 0.00	Trate/DT_{Cant} : r = 0.61, p-value = 0.00
Trate/F_{Cant} : r = 0.97, p-value = 0.00	Trate/F_{Cant} : r = 0.52, p-value = 0.00
Box OVIDE to sills	**Box OVIDE to sills**
Trate/DT_{Cant} : r = 0.32, p-value = 0.02	Trate/DT_{Cant} : r = 0.76, p-value = 0.00
Trate/F_{Cant} : r = 0.95, p-value = 0.00	Trate/F_{Cant} : r = 0.22, p-value = 0.12

<u>Table 6</u>: Correlation coefficient (r) and p-value between the divergence of Cant transport (DT_{Cant}) and the incoming (in) or outgoing (out) transport of Cant (T_{Cant}) for the three boxes, 25°N-36°N, 36°N-OVIDE and OVIDE-Sills, over the period 1959-2011. DT_{Cant} = incoming – outgoing Cant fluxes across the boundaries of boxes. Linear trend is removed from each times series beforehand.

Box 25° N to 36°N
${}^{in}T_{Cant}/DT_{Cant}$: r = 0.51, p-value = 0.00
${}^{out}T_{Cant}/DT_{Cant}$: r = -0.31, p-value = 0.03
Box 36°N to OVIDE
${}^{in}T_{Cant}/DT_{Cant}$: r = 0.79, p-value = 0.00
${}^{out}T_{Cant}/DT_{Cant}$: r = 0.07, p-value = 0.62
Box OVIDE to sills
${}^{in}T_{Cant}/DT_{Cant}$: r = 0.68, p-value = 0.00
${}^{out}T_{Cant}/DT_{Cant}$: r = -0.05, p-value = 0.70

Figures captions

Fig. 1: Column inventory (molC m^{-2}) of anthropogenic carbon for the year 2010: (a) model output and (b) Khatiwala et al. [2009].

Fig. 2: The Greenland-Portugal OVIDE and 24.5°N sections: observational data set (red points) and ORCA05-PISCES (black thick line).

Fig. 3: Anthropogenic C budget of the Subtropical and Subpolar North Atlantic regions over the

period 2003-2011. Average values and their standard deviations were estimated from smoothed time series. The horizontal arrows show the lateral Cant transport in PgC yr^{-1} (black font). Red numbers in the panel indicate the Cant storage rate in PgC yr^{-1}. The vertical arrows show the total (blue font) and anthropogenic (black font) air-sea CO_2 fluxes in PgC yr^{-1}. Green numbers represent the heat transport across sections in PW. Boundaries and surface area (m^2) of each box are indicated below the panels.

Fig. 4. Cumulative volume transport in Sv. (a) Vertically integrated transport from bottom to each specific density level (σ_1 with 0.01 kg m^{-3} resolution). Note that the sign of the profile has been changed. (b) Surface-to-bottom integrated transport cumulated from Greenland to Portugal (km). Model outputs for the month of June over the period 2002-10 (continuous line for mean value; shadows for confidence interval) are compared to estimates derived from OVIDE (dashed lines). On panel (a) the black horizontal lines indicate the density of MOC maximum corresponding to the separation between the upper (red) and lower (blue) limbs of MOC, in the model (σ_{MOC} = 32.02±0.05 kg m^{-3}, black continuous line) and observation-based assessments (σ_{MOC} = 32.14 kg m^{-3}, Zunino et al., 2014; black dashed line). The position of the Western limit of the NAC as observed from model simulations (dashed line) and from OVIDE data set (dashed-dotted line) as well as the Irminger current are indicated on panel (b).

Fig. 5 : Water column distribution of anthropogenic C concentrations (µmol kg^{-1}) along the Greenland-Portugal OVIDE section in June 2002: (a) model output and (b) as estimated from the OVIDE data set. The mean and standard deviation of the differences between these two assessments (model – OVIDE) over the OVIDE period (June 2002-04-06-08-10) are displayed on Fig. c and d. Black continuous and dashed lines indicate the limit between the upper and the lower limbs of the MOC in the model and the OVIDE data set.

Fig. 6: Zonally integrated volume transport (Sv) at 25°N computed either (a) for main water masses between January and March 2011 or (b) for density level (σ_1 with 0.1 kg m^{-3} resolution) over the year 2011 from model output. Main water masses identified at this latitude are North Atlantic Central Water (NACW) Antarctic Intermediate Water (AAIW) and Mediterranean Water (MW), which constitute the upper limb of the MOC (red), as well as North Atlantic Deep Water) and Antarctic Bottom Water (AABW), which compose the lower limb of the MOC (blue). Results from panel (a) are compared to observation-based estimates from Hernández-Guerra et al. (2014) (hatched bar plot). On panel (b) the black horizontal lines indicate the density of MOC maximum

corresponding to the separation of both limb in the model (σ_1 = 32.05 from July to September and σ_1 = 21.95 other months).

Fig. 7: Water column distribution of anthropogenic C concentrations (µmol kg^{-1}) along 24.5°N-25°N during winter (JFM) 2011: (a) model output and (b) as estimated from the 24.5N-data set. (c) Difference between both assessments (model – observation) in 2011. Black continuous and dashed lines indicate the limit between the upper and the lower limbs of the MOC in the model and the observation data set.

Fig. 8: (a-b) averaged total air-sea CO_2 fluxes (mol m^2 yr^{-1}) and month during which (c-d) the maximum or (e-f) the minimum value is reached in the North Atlantic Ocean over the period 2003-2011 as simulated by ORCA05-PISCES (a-c-e) and compared to the observation-based product of Landschützer et al. (2015a) (b-d-f). Black lines delimitate both boxes, 25°N-OVIDE and OVIDE sills.

Fig. 9: Interannual variability of total air-sea CO_2 fluxes (mol m^2 yr^{-1}) for the period 1982-2011 computed as the time series of its standard deviation: (a) ORCA05-PISCES and (b) the observation-based product of Landschützer et al. (2015a). Black lines delimitate both boxes, 25°N-OVIDE and OVIDE sills.

Fig. 10: Simulated annual time series of MOC magnitude (MOCσ, Sv) and transport of heat (PW) and anthropogenic C (PgC yr^{-1}) at at 25°N, 36° N and at the OVIDE section estimated over the period 1958-2012.

Fig. 11 : Simulated annual time series of anthropogenic carbon (Cant) budget (Pg yr^{-1}) from 25°N to 36°N bottom), from 36°N to OVIDE section (middle) and from OVIDE section to Greenland-Iceland-Scotland sills (top) over the period 1959-2011. Each budget is composed by the storage rate of Cant (red line), the air-sea flux of Cant (black dashed line) and the transport divergence of Cant (black full line).

Fig. 12: Distribution of mass transport integrated into density (sigma 1) layers with a 0.3 kg m^{-3} resolution for 25°N, 36°N, OVIDE section and the Greenland-Iceland-Scotland sills over the period 1958-2012 (colorbar). Dashed lines indicate the density limits of three major oceanic water class : Class 1N = northward North Atlantic Central Water; Class 1N = southward North Atlantic Central

Water ; Class 2 = Intermediate waters; Class 3 : North Atlantic Deep Water.

Fig. 13 : Simulated anthropogenic C budget (PgC yr-1) between 25°N and the Greenland-Iceland-Scotland sills over the period 1958-1994. Horizontal arrows represent the transport of Cant by NACW (purpose), IW (red) and NADW (blue) across 25°N, 36°N, OVIDE and sills. Grey vertical arrows show anthropogenic air-sea CO2 fluxes for each box whereas orange values indicate Cant storage rate. Black vertical arrows represent the deduced vertical transport of Cant between two Classes.

Fig. 14: Annual time series of the anomaly of mass transport (Sv, bar plot) compared to the winter NAO over the period 1959-2011 for (a) Class 1 at 36°N ($r = 0.55$, p-value = 0.00) and (b) Class 3 at OVIDE ($r = 55$, p-value = 0.00). Winter NAO index is index provided by the Climate Analysis Section (Hurrell and NCAR, https://climatedataguide.ucar.edu/climate-data/hurrell-north-atlantic-oscillation-nao-index-station-based).

Fig. 15: Simulated annual averaged transport of Cant by NACW (purpose), IW (red) and NADW (blue) across 25°N, 36°N, the OVIDE section and the Greenland-Iceland-Scotland sills (a) before and (b) between 1996 and 2012

Fig. 16: Simulated annual averaged temperature of mixed layer between 36°N and the OVIDE section (red line) and between the OVIDE section and the Greenland-Iceland-Scotland sills (black line) as simulated by the model over the period 1958-2012.

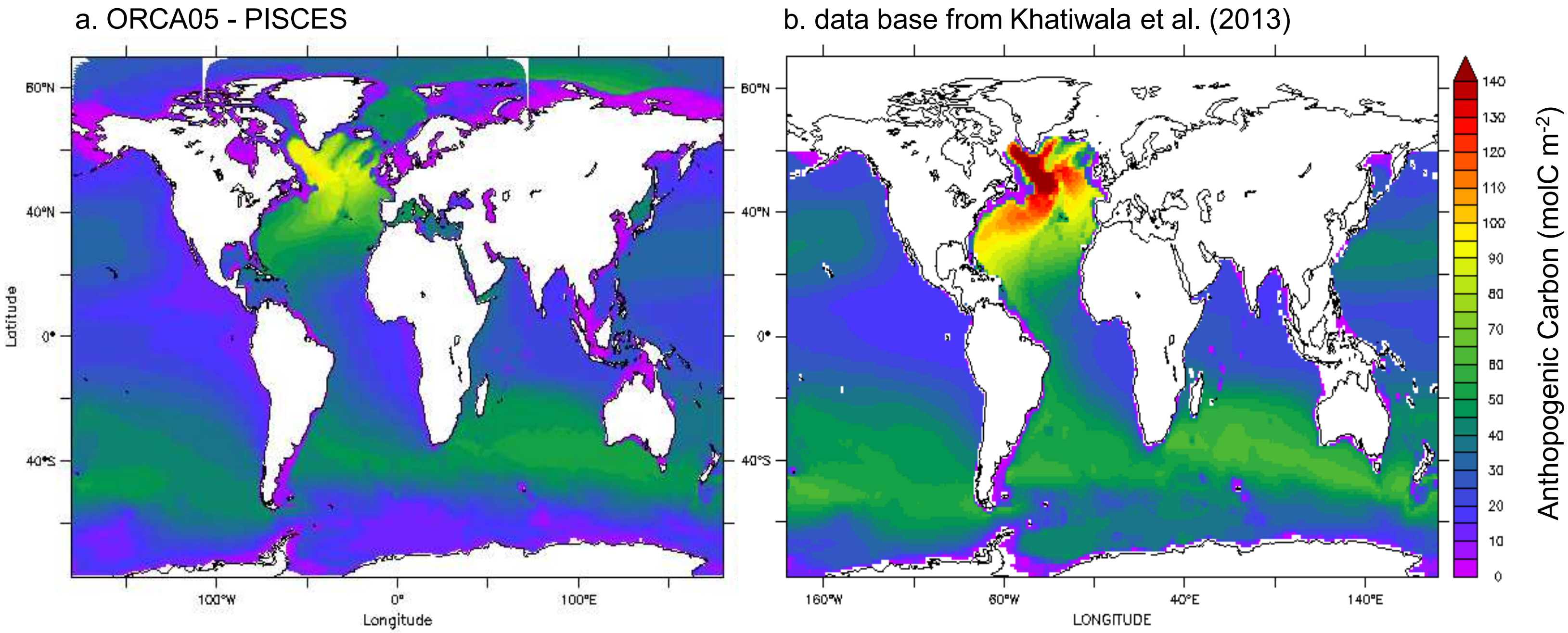

Fig. 1: Column inventory (molC m-2) of anthropogenic carbon for the year 2010: (a) model output and (b) Khatiwala et al. [2009].

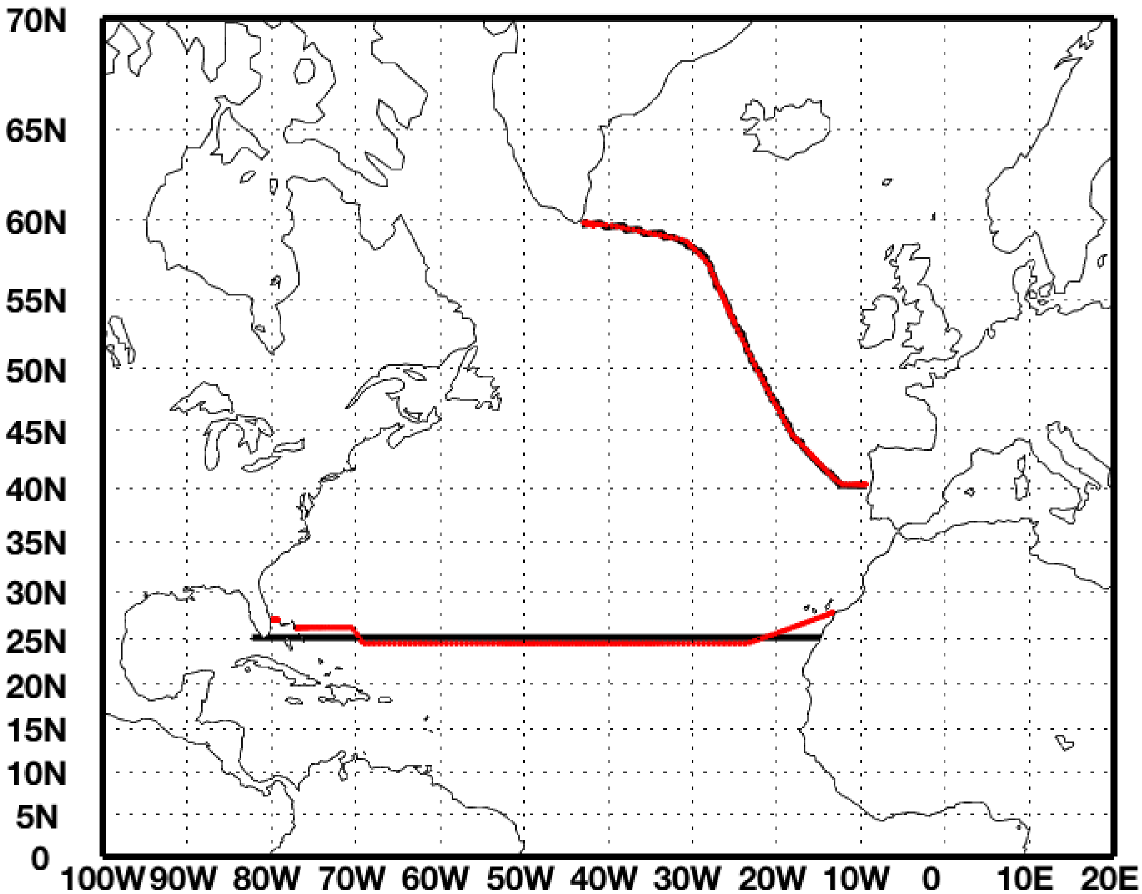

Fig. 2: The Greenland-Portugal OVIDE and 24.5°N sections: observational data set (red points) and ORCA05-PISCES (black thick line).

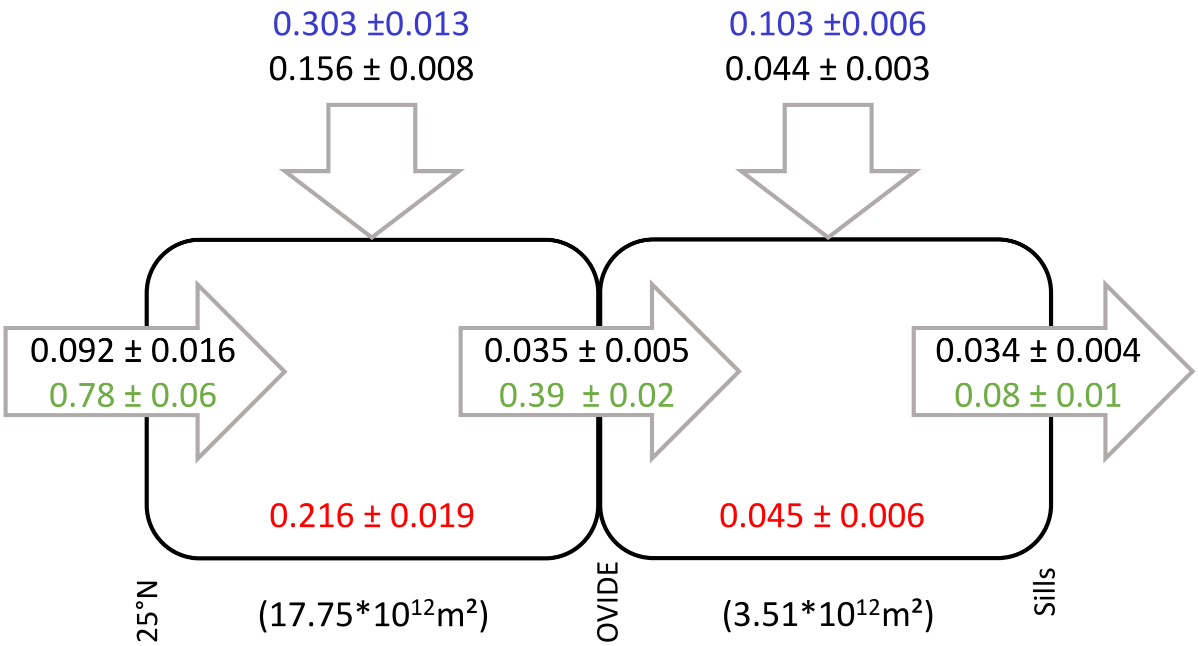

Fig. 3: Anthropogenic C budget of the Subtropical and Subpolar North Atlantic regions over the period 2003-2011. Average values and their standard deviations were estimated from smoothed time series. The horizontal arrows show the lateral Cant transport in PgC yr^{-1} (black font). Red numbers in the panel indicate the Cant storage rate in PgC yr^{-1}. The vertical arrows show the total (blue font) and anthropogenic (black font) air-sea CO_2 fluxes in PgC yr^{-1}. Green numbers represent the heat transport across sections in PW. Boundaries and surface area (m²) of each box are indicated below the panels. h.

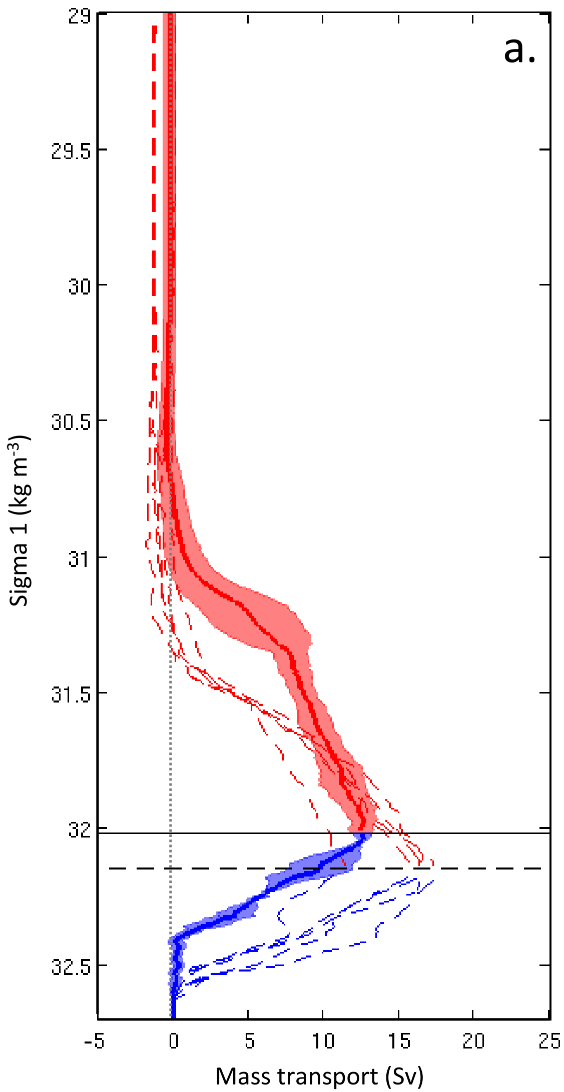

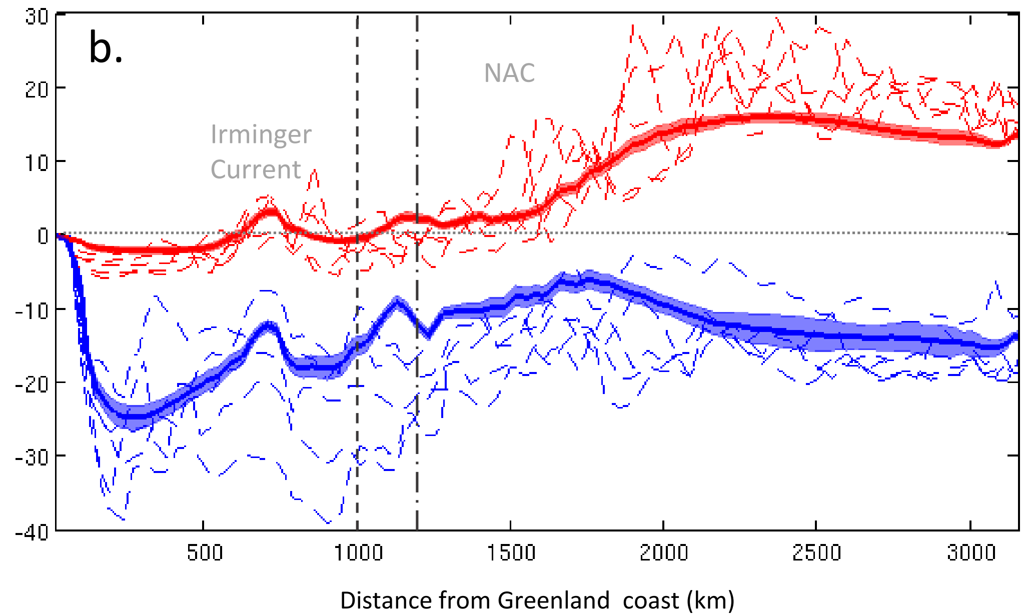

Fig. 4. Vertically integrated cumulative mass transport (Sv): model output for the month of June over the period 2002-10 (continuous line for mean value; shaded band for confidence interval) (a) from bottom to each specific density level (σ_1 with 0.01 kg m^{-3} resolution), note that the sign of the profile has been changed, and (b) from Greenland to Portugal (km) compared to estimates derived from OVIDE (dashed lines). On panel (a) the black horizontal lines indicate the density of MOCσ maximum corresponding to the separation between the upper (red) and lower (blue) limbs of MOC, in the model (σ_{MOC} = 32.02 ± 0.05 kg m^{-3}, black continuous line) and observation-based assessments (σ_{MOC} = 32.14 kg m^{-3}, Zunino et al., 2014; black dashed line). On panel (b) the position of the Western and Eastern NAC branches as well as the Irminger current, a NAC modified branch, are indicated in grey (Mercier et al., 2015).

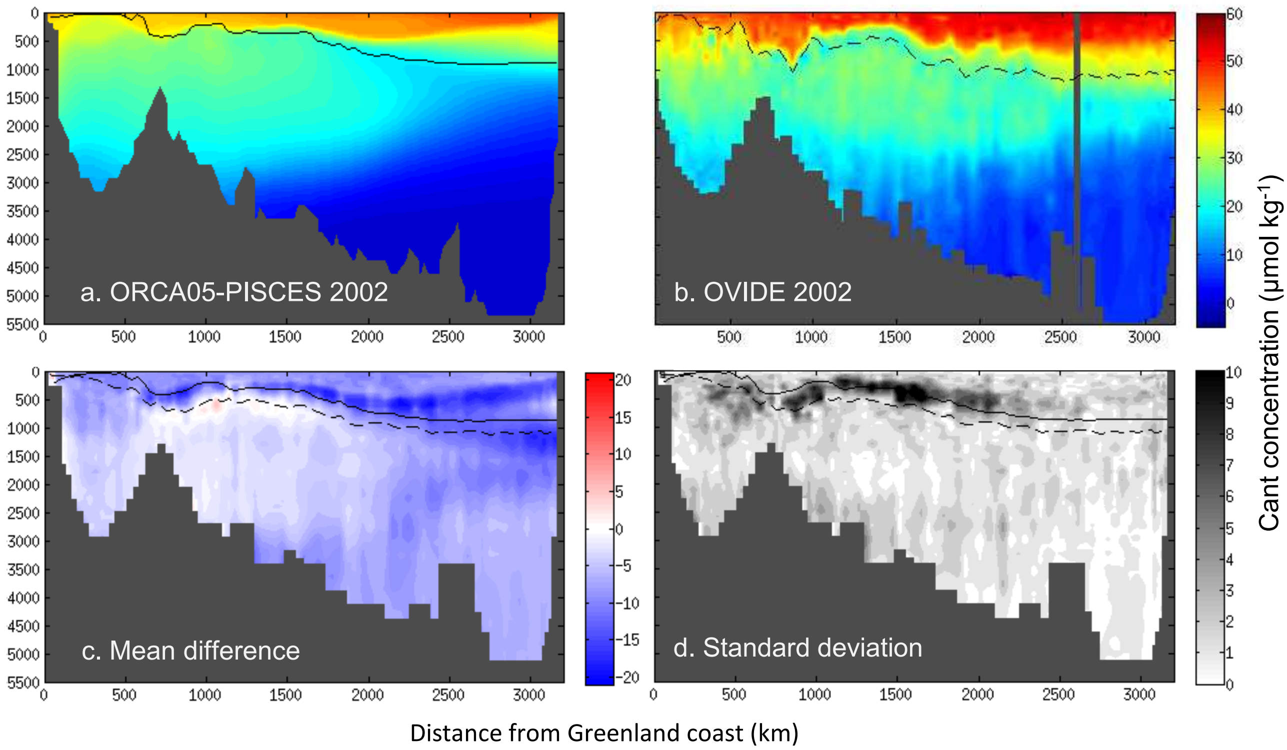

Fig. 5 : Water column distribution of anthropogenic C concentrations (µmol kg^{-1}) along the Greenland-Portugal OVIDE section in June 2002: (a) model output and (b) as estimated from the OVIDE data set. The mean and standard deviation of the differences between these two assessments (model – OVIDE) over the OVIDE period (June 2002-04-06-08-10) are displayed on Fig. c and d. Black continuous and dashed lines indicate the limit between the upper and the lower limbs of the MOC in the model and the OVIDE data set.

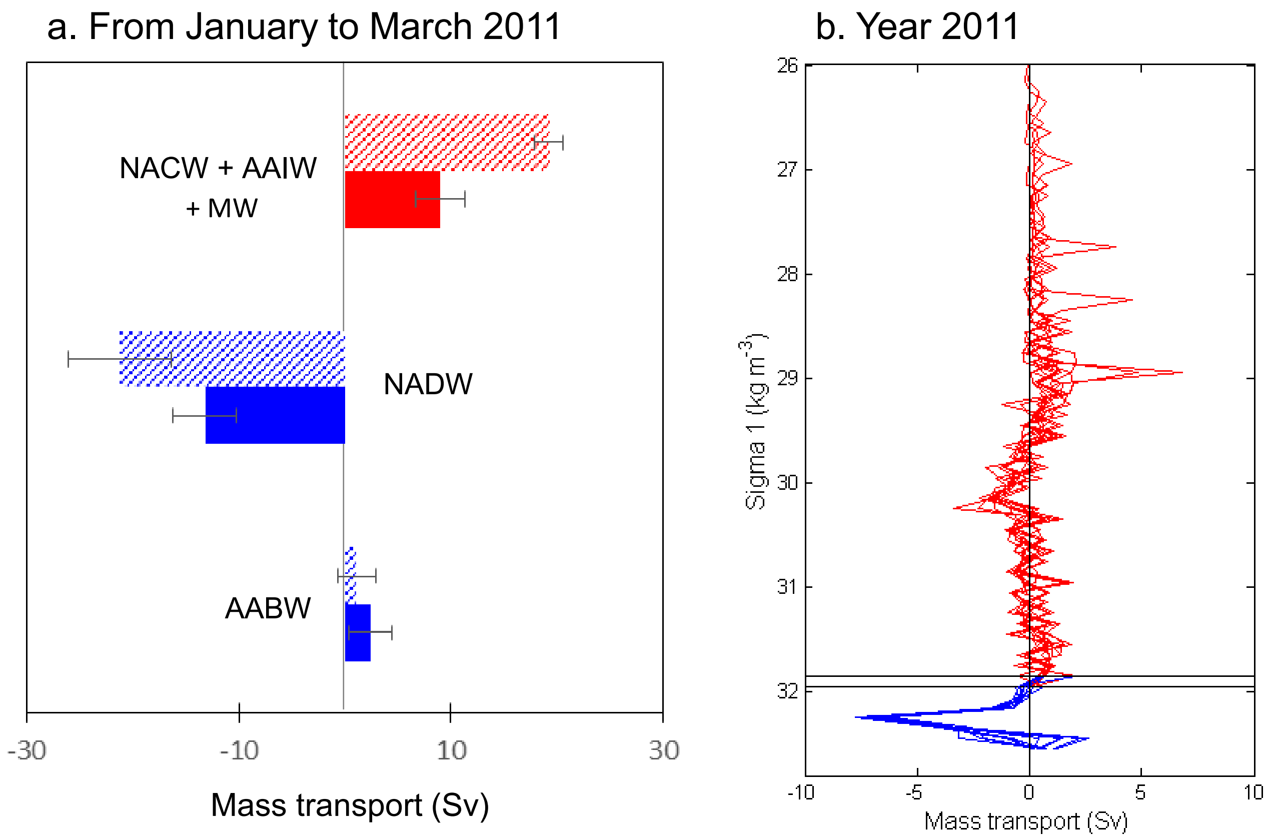

Fig. 6: Zonally integrated volume transport (Sv) at 25°N computed either (a) for main water masses between January and March 2011 or (b) for density level (σ1 with 0.1 kg m^{-3} resolution) over the year 2011 from model output. Main water masses identified at this latitude are North Atlantic Central Water (NACW), Antarctic Intermediate Water (AAIW) and Mediterranean Water (MW), which constitute the upper limb of the MOC (red), as well as North Atlantic Deep Water) and Antarctic Bottom Water (AABW), which compose the lower limb of the MOC (blue). Results from panel (a) are compared to observation-based estimates from Hernández-Guerra et al. (2014) (hatched bar plot). On panel (b) the black horizontal lines indicate the density of MOC maximum corresponding to the separation of both limb in the model (σ1 = 32.05 from July to September and σ1 = 21.95 other months).

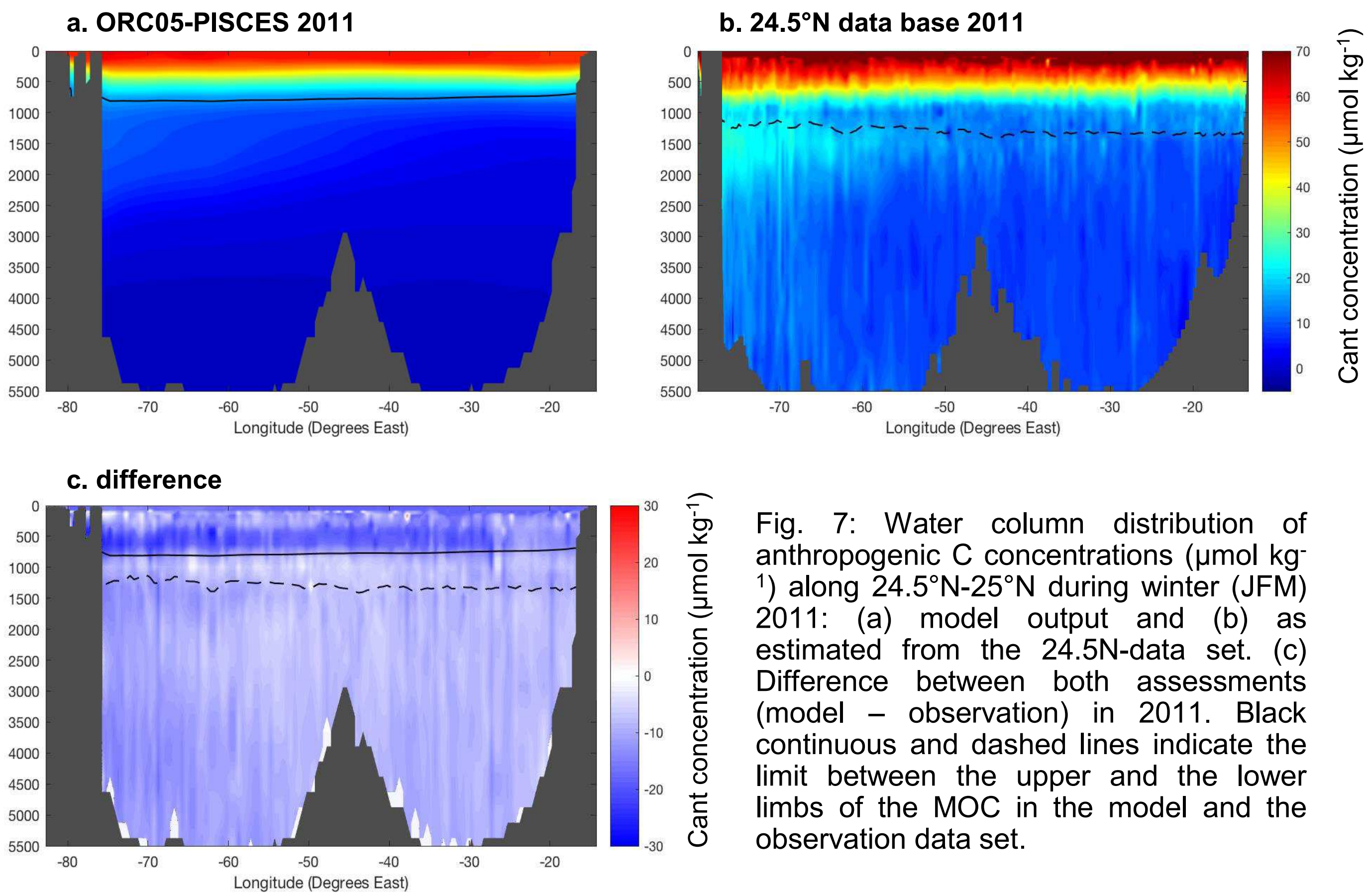

Fig. 7: Water column distribution of anthropogenic C concentrations (µmol kg^{-1}) along 24.5°N-25°N during winter (JFM) 2011: (a) model output and (b) as estimated from the 24.5N-data set. (c) Difference between both assessments (model – observation) in 2011. Black continuous and dashed lines indicate the limit between the upper and the lower limbs of the MOC in the model and the observation data set.

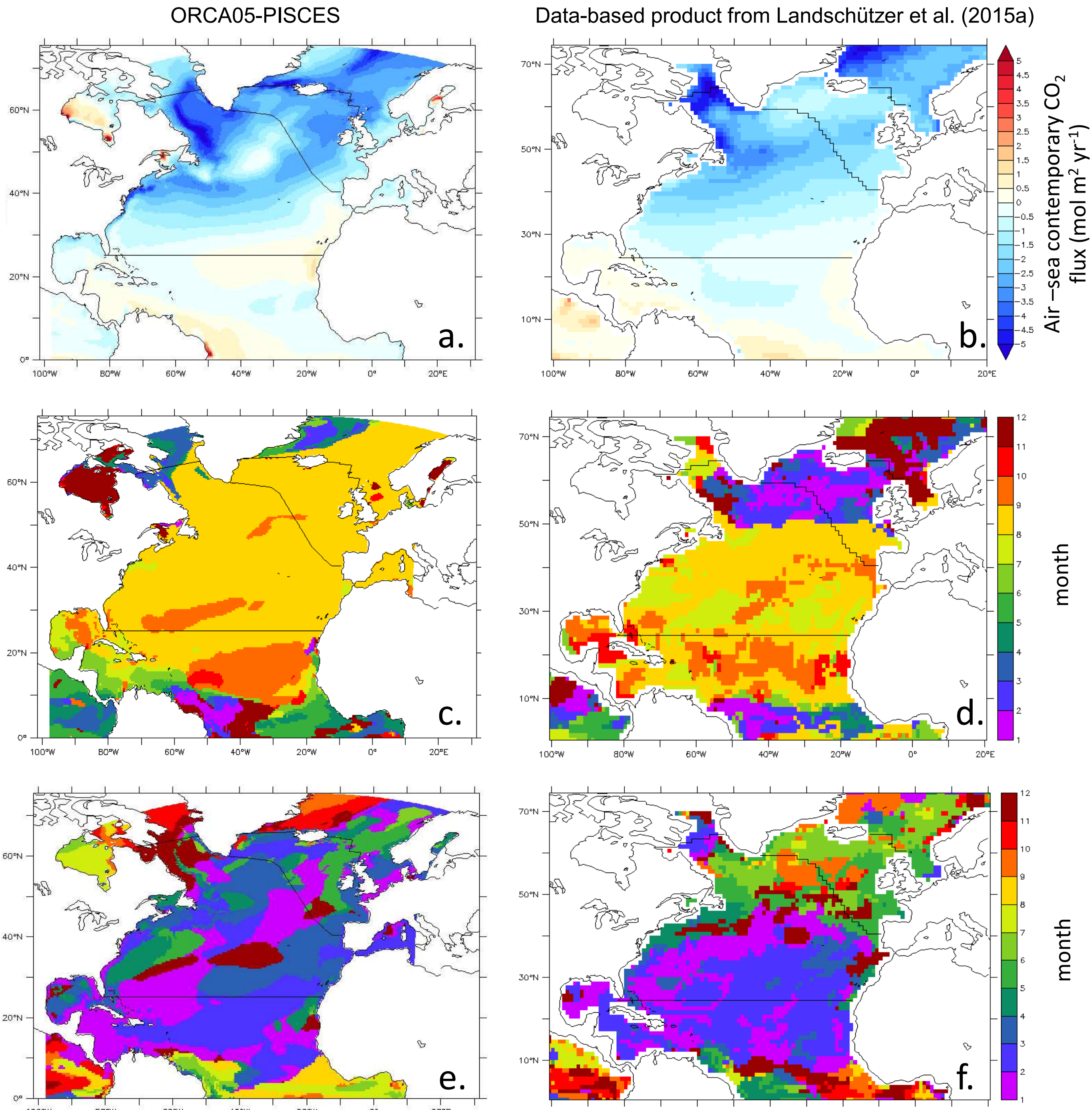

Fig. 8: (a-b) averaged total air-sea CO_2 fluxes (mol m^2 yr^{-1}) and month during which (c-d) the maximum or (e-f) the minimum value is reached in the North Atlantic Ocean over the period 2003-2011 as simulated by ORCA05-PISCES (a-c-e) and compared to the observation-based product of Landschützer et al. (2015a) (b-d-f). Black lines delimitate both boxes, 25°N-OVIDE and OVIDE sills.

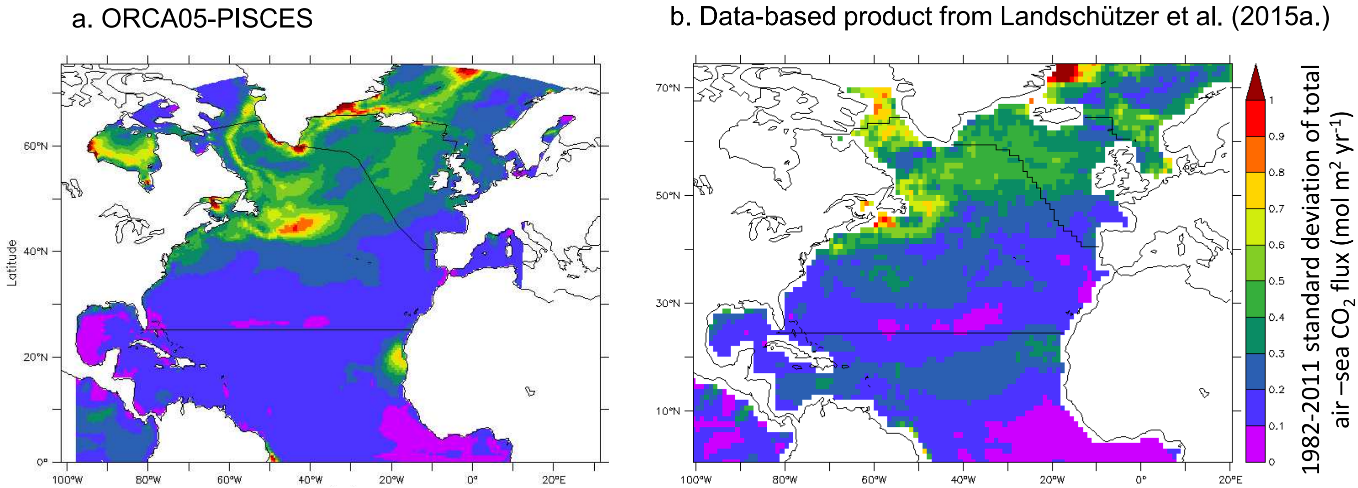

Fig. 9: Interannual variability of total air-sea CO_2 fluxes (mol m^2 yr^{-1}) for the period 1982-2011 computed as the time series of its standard deviation: (a) ORCA05-PISCES and (b) the observation-based product of Landschützer et al. (2015a). Black lines delimitate both boxes, 25°N-OVIDE and OVIDE sills.

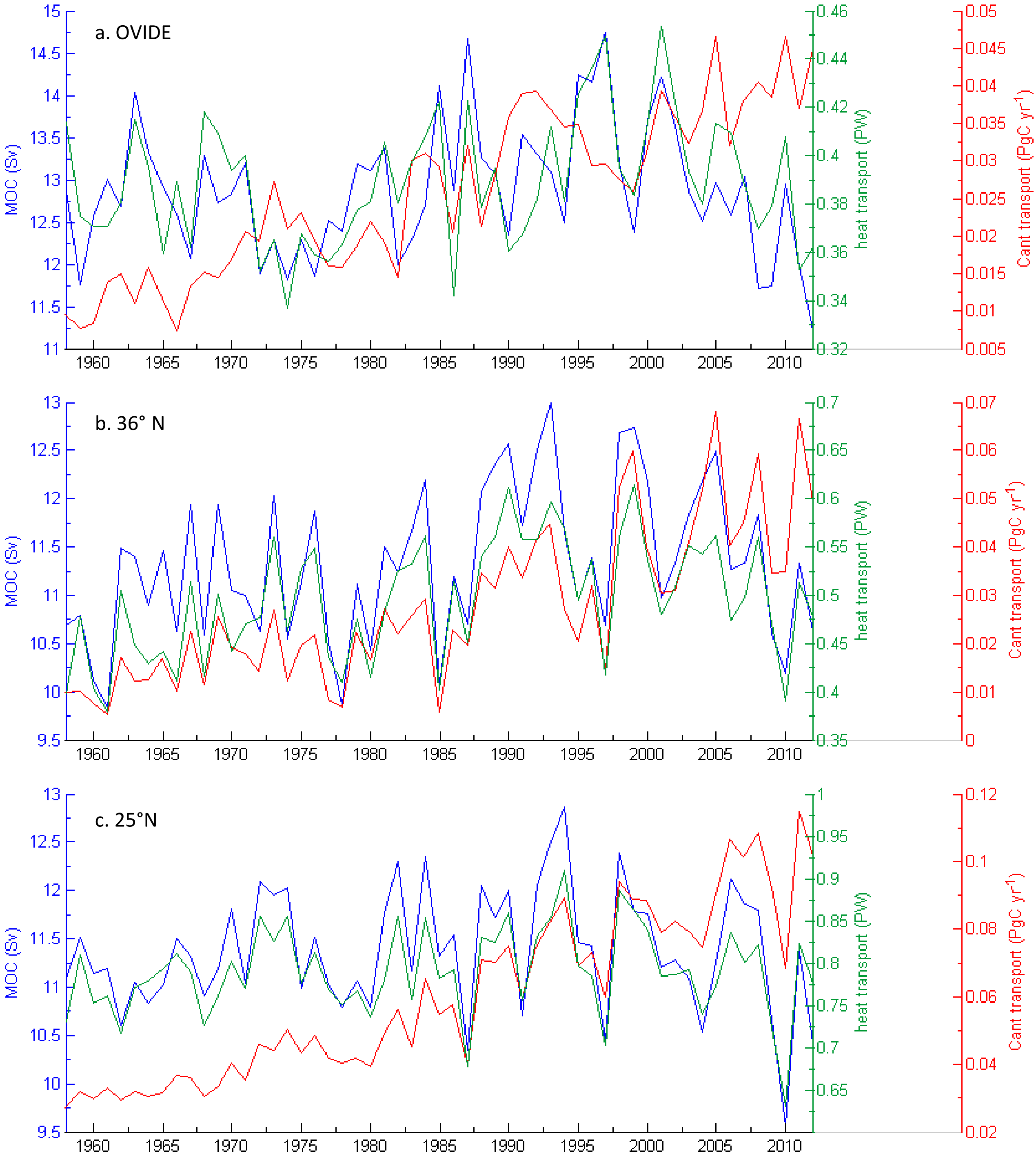

Fig. 10: Simulated 1958-2012 annual time series of the magnitude of the MOC (Sv), the transport of heat (PW) and the transport of Cant (PgC yr^{-1}) through (a) the OVIDE section, (b) 36° N and © 25°N.

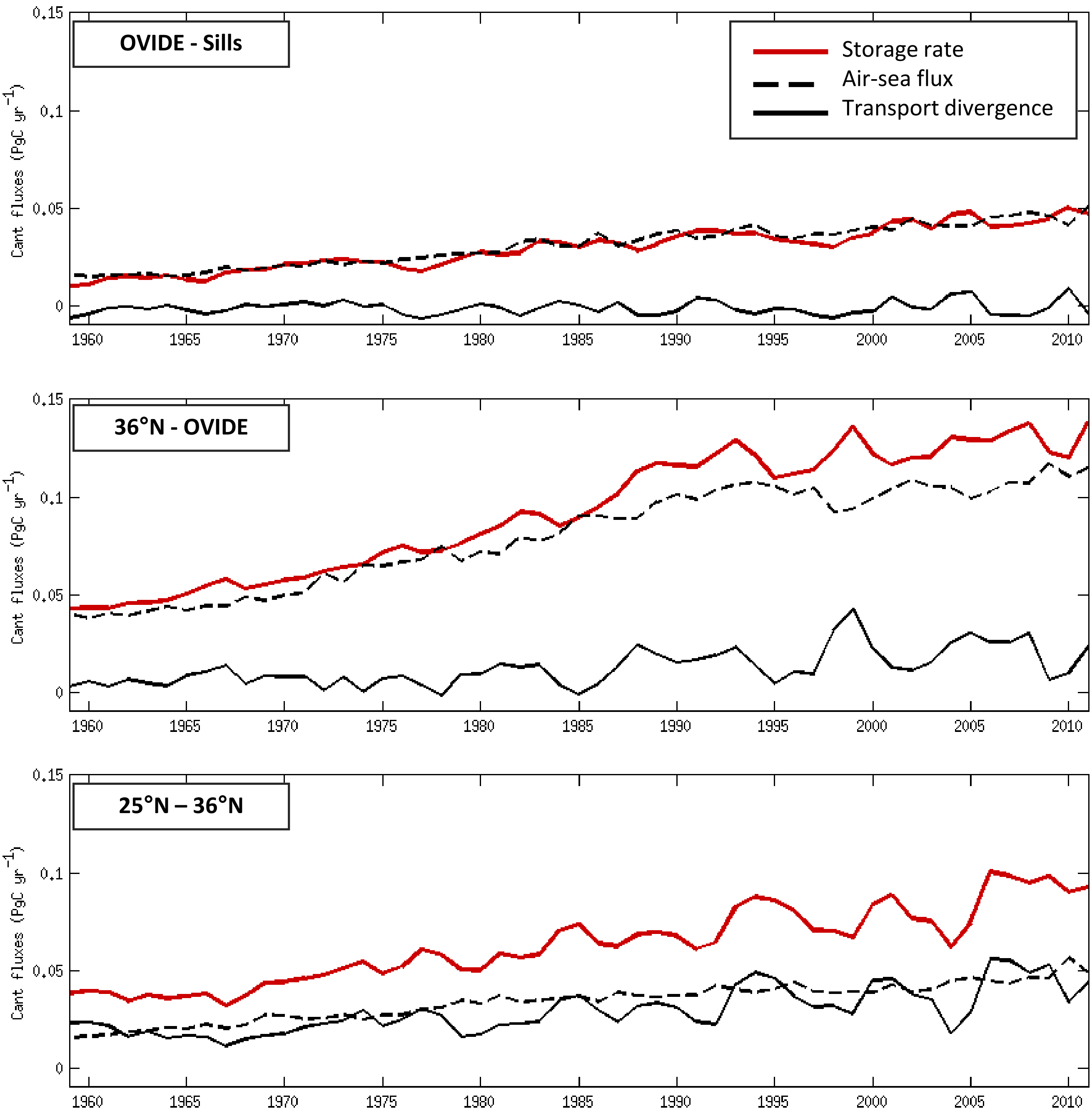

Fig. 11 : Simulated annual time series of anthropogenic carbon (Cant) budget (Pg yr-1) from 25°N to 36°N bottom), from 36°N to OVIDE section (middle) and from OVIDE section to Nordic sills (top) over the period 1959-2011. Each budget is composed by the storage rate of Cant (red line), the air-sea flux of Cant (black dashed line) and the transport divergence of Cant (black full line).

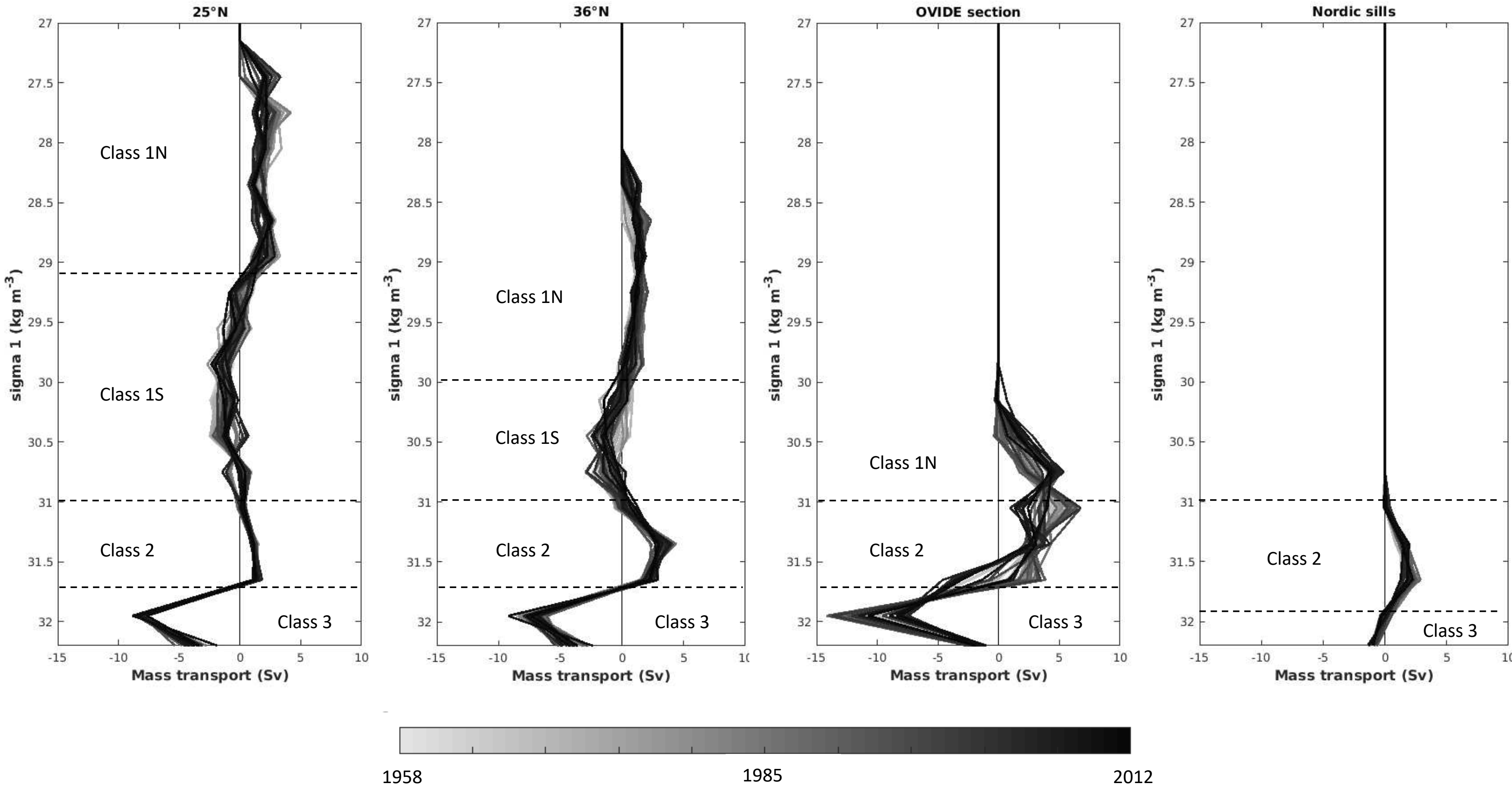

Fig. 12: Distribution of mass transport integrated into density (sigma 1) layers with a 0.3 kg m^{-3} resolution for 25°N, 36°N, OVIDE section and the Nordic sills over the period 1958-2012 (colorbar). Dashed lines indicate the density limits of three major oceanic water class : Class 1N = northward North Atlantic Central Water; Class 1S = southward North Atlantic Central Water ; Class 2 = Intermediate waters; Class 3 : North Atlantic Deep Water.

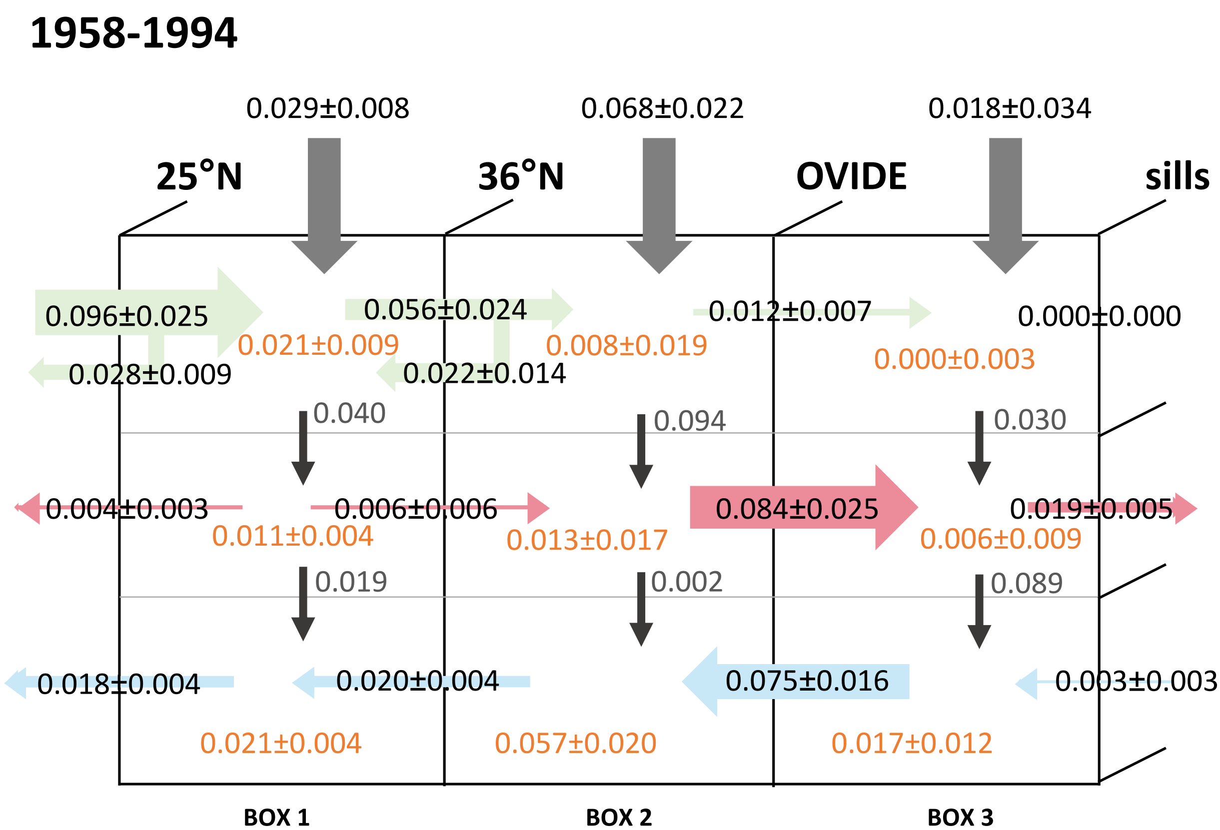

Fig. 13 : Simulated anthropogenic C budget (PgC yr^{-1}) between 25°N and the Greenland-Iceland-Scotland sills over the period 1958-1994. Horizontal arrows represent the transport of Cant by NACW (purpose), IW (red) and NADW (blue) across 25°N, 36°N, OVIDE and sills. Grey vertical arrows show anthropogenic air-sea CO_2 fluxes for each box whereas orange values indicate Cant storage rate. Black vertical arrows represent the deduced vertical transport of Cant between two Classes.

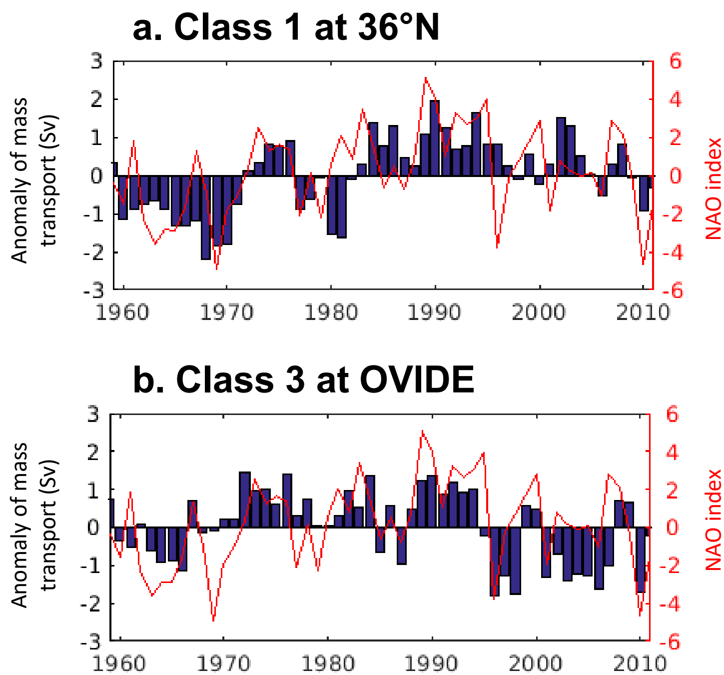

Fig. 14 : Annual time series of the anomaly of mass transport (Sv, bar plot) compared to the winter NAO over the period 1959-2011 for (a) Class 1 at 36°N (r = 0.55, p-value = 0.00) and (b) Class 3 at OVIDE (r = 55, p-value = 0.00). Winter NAO index is index provided by the Climate Analysis Section (Hurrell and NCAR, https://climatedataguide.ucar.edu/climate-data/hurrell-north-atlantic-oscillation-nao-index-station-based).

1996-2012

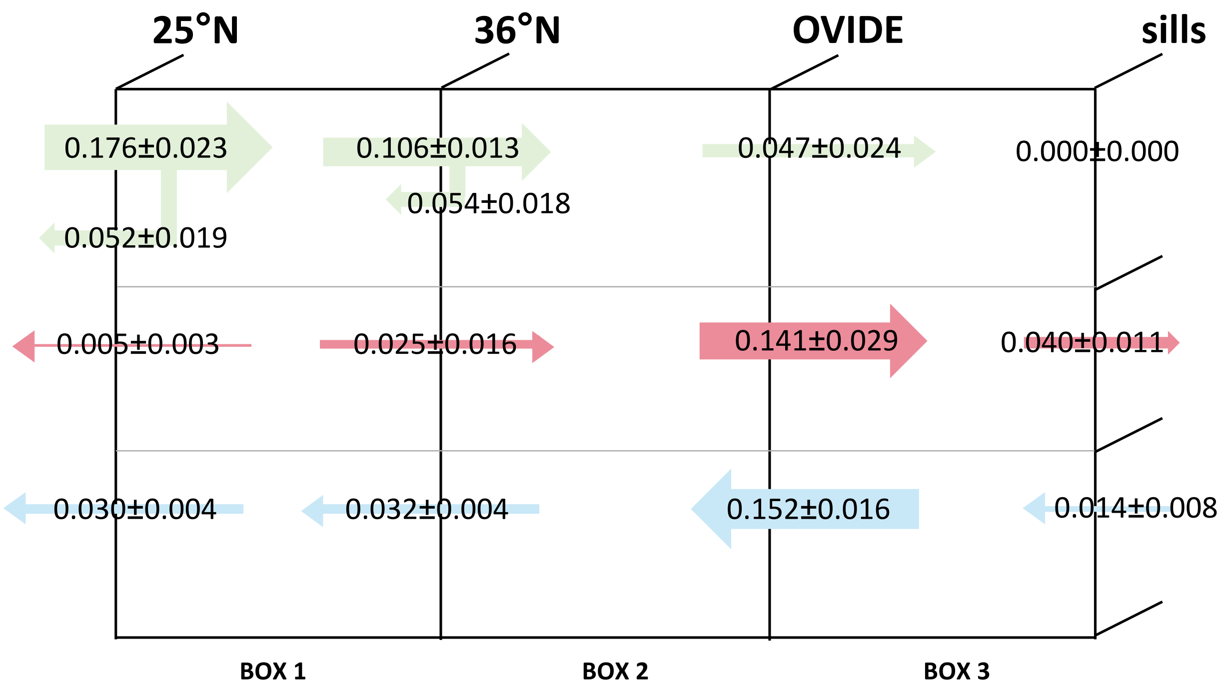

Fig. 15: Simulated annual averaged transport of Cant by NACW (purpose), IW (red) and NADW (blue) across 25°N, 36°N, the OVIDE section and the Greenland-Iceland-Scotland sills (a) before and (b) between 1996 and 2012.

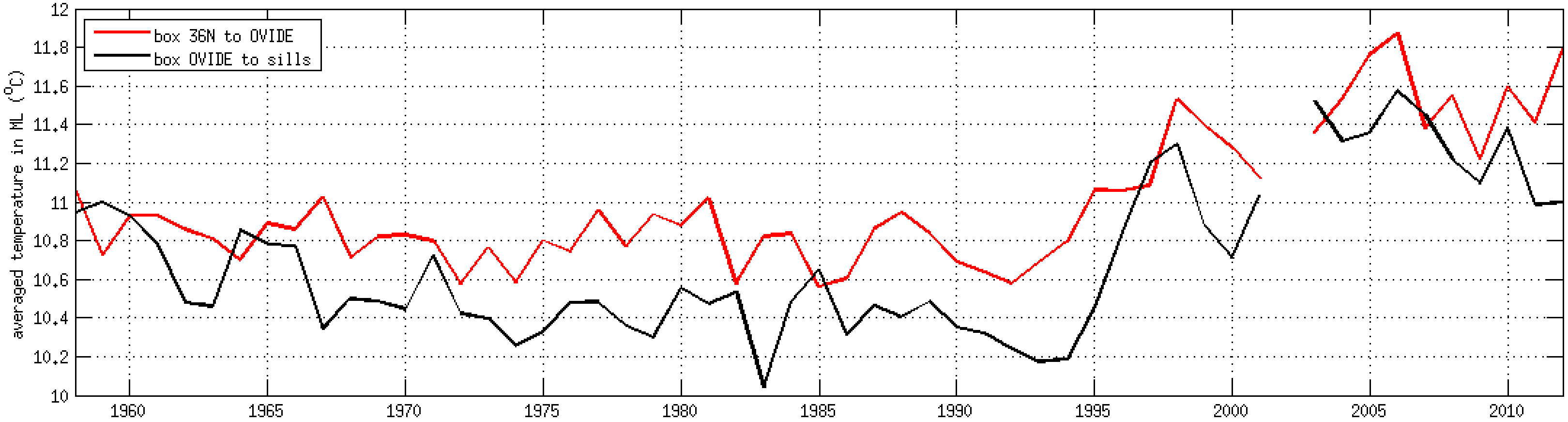

Fig. 16: Simulated annual averaged temperature of mixed layer between 36°N and the OVIDE section (red line) and between the OVIDE section and the Nordic sills (black line) as simulated by the model over the period 1958-2012.